2011-06

Electrochemical studies of passive film formation and corrosion of friction stir processed nickel aluminum bronze

LeGrand, Peggy S.

Monterey, California. Naval Postgraduate School

NAVAL POSTGRADUATE SCHOOL

MONTEREY, CALIFORNIA

THESIS

ELECTROCHEMICAL STUDIES OF PASSIVE FILM FORMATION AND CORROSION OF FRICTION STIR PROCESSED NICKEL ALUMINUM BRONZE

by

Peggy Sue LeGrand

June 2011

Thesis Advisor:	Joseph Farmer
Second Reader:	Luke Brewer

Approved for public release; distribution is unlimited

THIS PAGE INTENTIONALLY LEFT BLANK

REPORT DOCUMENTATION PAGE			*Form Approved OMB No. 0704-0188*
Public reporting burden for this collection of information is estimated to average 1 hour per response, including the time for reviewing instruction, searching existing data sources, gathering and maintaining the data needed, and completing and reviewing the collection of information. Send comments regarding this burden estimate or any other aspect of this collection of information, including suggestions for reducing this burden, to Washington headquarters Services, Directorate for Information Operations and Reports, 1215 Jefferson Davis Highway, Suite 1204, Arlington, VA 22202-4302, and to the Office of Management and Budget, Paperwork Reduction Project (0704-0188) Washington DC 20503.			
1. AGENCY USE ONLY ***(Leave blank)***	**2. REPORT DATE** June 2011	**3. REPORT TYPE AND DATES COVERED** Master's Thesis	
4. TITLE AND SUBTITLE Electrochemical Studies of Passive Film Formation and Corrosion of Friction Stir Processed Nickel Aluminum Bronze			**5. FUNDING NUMBERS**
6. AUTHOR(S) ENS Peggy S. LeGrand			
7. PERFORMING ORGANIZATION NAME(S) AND ADDRESS(ES) Naval Postgraduate School Monterey, CA 93943-5000			**8. PERFORMING ORGANIZATION REPORT NUMBER**
9. SPONSORING /MONITORING AGENCY NAME(S) AND ADDRESS(ES) N/A			**10. SPONSORING/MONITORING AGENCY REPORT NUMBER**
11. SUPPLEMENTARY NOTES The views expressed in this thesis are those of the author and do not reflect the official policy or position of the Department of Defense or the U.S. Government. IRB Protocol number: N/A.			
12a. DISTRIBUTION / AVAILABILITY STATEMENT Approved for public release; distribution is unlimited			**12b. DISTRIBUTION CODE**

13. ABSTRACT (maximum 200 words)

The Navy currently uses Nickel-Aluminum Bronze (NAB) for its propellers. Friction stir processing (FSP) is a proposed method of improving the mechanical properties of NAB, and it is believed to improve the corrosion-resistive properties of NAB. This thesis used multiple techniques to compare the corrosion resistance of as-cast NAB with FSP NAB. Passive films were grown on the as-cast (AC) and FSP samples and modeled in order to relate the impedance data to changes in phase and microstructure resulting from FSP of NAB. Impedance modeling provides a way of measuring the passive film that forms on a metal and protects it from corrosion. In addition, cyclic polarization data was taken in order to study the stability of the films over a range of potentials. This data was then compared with SEM images to link the changes in the passive films with the changes in microstructure that occurred due to FSP.

14. SUBJECT TERMS Friction Stir Processing, Nickel Aluminum Bronze, Propeller, Corrosion, Passive Film Formation			**15. NUMBER OF PAGES** 93
			16. PRICE CODE
17. SECURITY CLASSIFICATION OF REPORT Unclassified	**18. SECURITY CLASSIFICATION OF THIS PAGE** Unclassified	**19. SECURITY CLASSIFICATION OF ABSTRACT** Unclassified	**20. LIMITATION OF ABSTRACT** UU

NSN 7540-01-280-5500

Standard Form 298 (Rev. 2-89)
Prescribed by ANSI Std. 239-18

THIS PAGE INTENTIONALLY LEFT BLANK

Approved for public release; distribution is unlimited

ELECTROCHEMICAL STUDIES OF PASSIVE FILM FORMATION AND CORROSION OF FRICTION STIR PROCESSED NICKEL ALUMINUM BRONZE

Peggy S. LeGrand
Ensign, United States Navy
B.S., United States Naval Academy, 2011

Submitted in partial fulfillment of the
requirements for the degree of

MASTER OF SCIENCE IN MECHANICAL ENGINEERING

from the

NAVAL POSTGRADUATE SCHOOL
June 2011

Author: Peggy S. LeGrand

Approved by: Joseph Farmer, PhD
Thesis Advisor

Luke Brewer, PhD
Second Reader

Knox Millsaps, PhD
Chair, Department of Mechanical and Aerospace Engineering

THIS PAGE INTENTIONALLY LEFT BLANK

ABSTRACT

The Navy currently uses Nickel-Aluminum Bronze (NAB) for its propellers. Friction stir processing (FSP) is a proposed method of improving the mechanical properties of NAB, and it is believed to improve the corrosion-resistive properties of NAB. This thesis used multiple techniques to compare the corrosion resistance of as-cast NAB with FSP NAB. Passive films were grown on the as-cast (AC) and FSP samples and modeled in order to relate the impedance data to changes in phase and microstructure resulting from FSP of NAB. Impedance modeling provides a way of measuring the passive film that forms on a metal and protects it from corrosion. In addition, cyclic polarization data was taken in order to study the stability of the films over a range of potentials. This data was then compared with SEM images to link the changes in the passive films with the changes in microstructure that occurred due to FSP.

THIS PAGE INTENTIONALLY LEFT BLANK

TABLE OF CONTENTS

THIS PAGE INTENTIONALLY LEFT BLANK

LIST OF FIGURES

LIST OF TABLES

THIS PAGE INTENTIONALLY LEFT BLANK

LIST OF ACRONYMS AND ABBREVIATIONS

AC – As-Cast
BCC –Body Centered Cubic
CP – Cyclic Polarization
EIS – Electrochemical Impedance Spectroscopy
FCC – Face Centered Cubic
FSP – Friction Stir Processing
HAZ – Heat Affected Zone
IMP – Inches Per Minute
NAB – Nickel Aluminum Bronze
OCP – Open Circuit Corrosion Potential
RPM –Rotations Per Minute
SPC – Selective Phase Corrosion
SZ – Stir Zone
TMAZ –Thermo-mechanically Affected Zone
TWI – The Welding Institute
USN – United States Navy

THIS PAGE INTENTIONALLY LEFT BLANK

ACKNOWLEDGMENTS

I would like to thank Dr. Joe Farmer for all of his efforts, patience, and pushing me to achieve more than I thought possible. Thank you for the encouragement and insight. I would like to thank Dr. Luke Brewer for all of the tough questions and Dr. Sarath Menon for the help with sample preparation.

To my roommates, I extend a warm thank you for all of your patience with me and help with Dog when I stayed in to finish my labs. Dog appreciated it too.

To Moose, thanks for the tail wagging and wet nose encouragement, help with typing, our late night adventures and forgiving me for staying late. You really kept me going this year and got me out of bed each day.

I would also like to thank Heather, for always being my voice of reason and giving me a new perspective. Liz, I thank you for always being positive and encouraging in tough times.

Additionally, I would like to thank my parents and siblings for giving me the motivation to keep going and the love to know that I can do anything with a lot of hard work and support.

I would also like to thank my bike for giving me the sanity to continue when I did not want to.

THIS PAGE INTENTIONALLY LEFT BLANK

I. INTRODUCTION

Nickel Aluminum Bronze (NAB) has been used as a propeller material by the United States Navy (USN) for many years. NAB's high strength, fracture toughness and ductility make it an ideal material for this application; however, due to the size of the propellers, casting is used as the main manufacturing process. During casting, the cooling rates of the NAB are very slow, which allow for porosity and a coarse microstructure [1].

The coarse microstructure and substantial porosity created in the casting process have deleterious effects on material performance, including strength, fracture toughness, and corrosion resistance [1]. As discussed by Pidaparti et al. [2], corrosion fatigue cracks can initiate at pits on the surface of NAB, since these pits serve as points of stress concentration. Friction stir processing (FSP) can be used for surface modification of the alloy, with corresponding improvements in performance. This process is similar to friction stir welding (FSW) but is used for the purpose of refining and homogenizing grain structure and reducing the size of near-surface pores from the as-cast condition. FSP creates a metallic surface finish with increased strength, ductility and corrosion resistance [3], thereby allowing for a reduction in repair time and an increase the service life of propellers.

While the relationship between microstructure and various physical and mechanical properties of NAB have been previously studied, virtually no quantitative corrosion studies of the impact of FSP on the passivity and corrosion resistance have been conducted. Since the service environment of propellers fabricated from NAB is seawater, the corrosion performance in seawater is of particular interest to the Navy.

THIS PAGE INTENTIONALLY LEFT BLANK

II. BACKGROUND

A. NICKEL ALUMINUM BRONZE

Nickel Aluminum Bronze (NAB) is a predominantly copper alloy that has been used as a propeller material for many years. NAB is corrosion, erosion and fatigue resistant; thus, it is ideal for use in marine environments. NAB is usually a two-phase alloy with 5 to 11% aluminum [4, 5]. Published compositions for NAB are summarized in Table 1 [4, 6].

Table 1. Composition of Nickel Aluminum Bronze (C95800) (wt. %), after [4, 6]

Ref.	Element	Cu	Al	Ni	Fe	Mn	Si	Pb
[4]	**Alloy – I**	80.0	9.4	4.9	4.4	1.2	0.07	NA
[4]	**Alloy – II**	80.1	9.0	4.4	5.1	1.4	0.07	NA
[6]	**Min-Max**	79.0	8.5-9.5	4.0-5.0	3.5-4.5	0.8-1.5	0.10 (max)	0.03 (max)
[6]	**Nominal**	81	9	5	4	1	----	----

Nickel and aluminum improve NAB's corrosion resistance, while iron helps raise the yield strength and acts as a grain refiner. The variations in the microstructure result in a wide range of seawater corrosion resistance. Pourbaix diagrams link alloying elements with passivity and corrosion resistance. The Pourbaix diagrams for copper, aluminum, nickel, and iron indicate the possible formation of Cu_2O, CuO, $Cu(OH)_2$, $Al_2O_3{\cdot}3H_2O$ (hydragillite), $Ni(OH)_2$ (nickelous hydroxide), Ni_3O_4 (nickel-nickelic oxide), Ni_2O_3 (nickelic oxide), NiO_2 (nickel peroxide), Fe_3O_4 (magnetite), Fe_2O_3 (haematite), $Fe(OH)_2$ (ferrous hydroxide), or $Fe(OH)_3$ at near neutral pH in pure water [7]. Crude approximations of the Pourbaix diagram for multi-component alloys can be approximated by overlaying the diagrams for the constituent elements. The aluminum oxide exhibits stability over the largest range of potential; therefore, it is believed that aluminum is

theconstituent responsible for imparting the greatest degree of passive film stability, followed by the oxides and hydroxides of nickel.

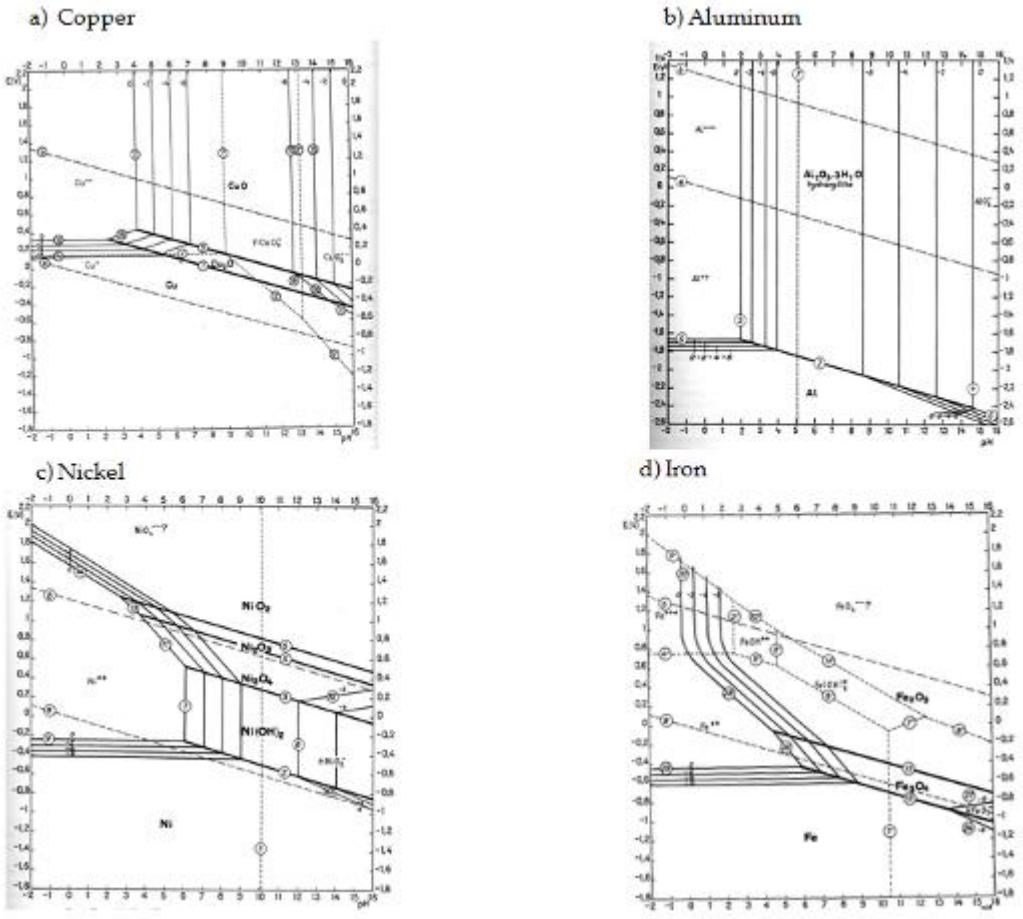

Figure 1. Potential-pH equilibrium diagrams for a) Cu, b) Al, c) Ni, d) Fe at 25 ˚C, from [7]

1. Phases

Phase formation in NAB is discussed by Hasan et al. [4]. These authors note that while NAB with a nominal composition of Cu with 5 wt. % Al, 5 wt. % Ni, 5 wt. % Fe is widely used for marine applications, it has variable corrosion resistance in seawater. This variability is explained in terms of its complex microstructure, which is affected by composition and thermal history (heat treatment). Under normal conditions, this alloy has a predominant Cu-rich solid-solution α-phase (FCC), several intermetallic kappa (κ)

phases (NiAl, Fe_3Al, and other aluminides), and some retained martensitic beta (β) phase. The phase diagram shown in Figure 2 for this material indicates that upon cooling at an aluminum composition of 9 wt. % Al, κ-phase formation begins below 930°C, with the disappearance of the β-phase below approximately 860°C.

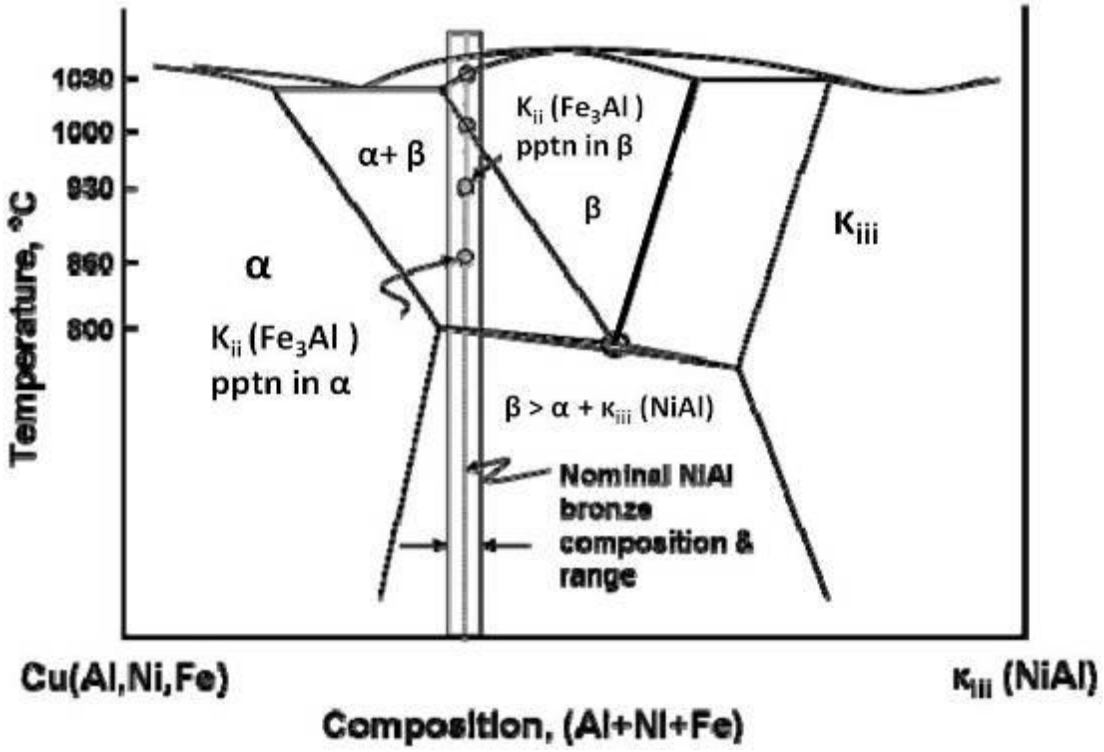

Figure 2. Vertical section of the Cu-Al-5Ni-5Fe equilibrium diagram, from [4]

NAB's properties are sensitive to the alloying elements of which it is composed. The resulting microstructure is controlled by the temperatures and cooling rates that occur during processing. In casting, NAB is poured into a mold, where it cools at an equilibrium rate of approximately 10^{-3} $^{o}Cs^{-1}$. As the casting cools, the NAB undergoes a transformation from liquid to β phase and finally to a combination of α, κ_{ii}, κ_{iii}, and κ_{iv} phases [8]. During FSP peak temperatures are between 800 and 1000 degrees Celsius, resulting in a two-phase region of α and β phases. Figure 3 shows the transformations that occur during cooling of NAB.

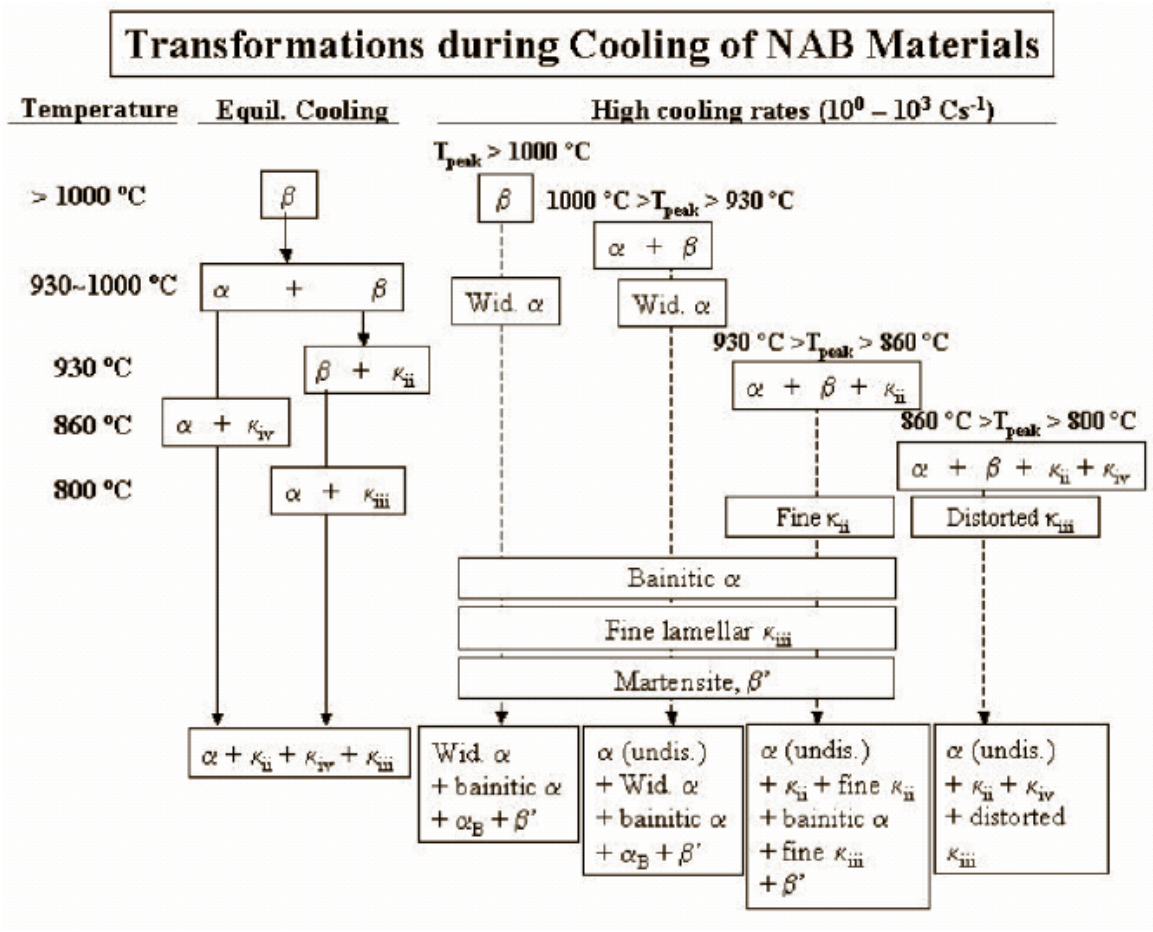

Figure 3. Transformation products of NAB during cooling, from [9]

The alpha (α), beta (β) and kappa (κ_{ii}, κ_{iii} and κ_{iv}) phases are described in further detail below.

The alpha (α) phase is a Cu-rich face centered cubic (FCC) structure. In castings at room temperature, the alpha phase makes up the majority of the cast NAB structure. Some of the α forms during the slow cooling process in the β phase and has a Widmanstätten morphology [9].

The beta (β) phase of NAB has a body centered cubic (BCC) structure and exists at high temperatures. During cooling, this phase can transform into various microstructures, which are dependent upon the cooling rate. If cooled slowly, the β can transform into one of several kappa phases which are described in the next section. If

quenched at a high cooling rate, the β can form a martensitic microstructure, while a more moderate cooling rate will form a bainitic microstructure [4].

There are four kappa (κ) phases in NAB, of which three are predominant. The kappa phases increase NAB's mechanical strength without causing any decrease in the ductility. Which phases are present depends on the amount of iron and aluminum present in the alloy.

The κ_i phase forms only when sufficient iron is present in the matrix. The κ_i phase is dendritic and defined by shape and location rather than microstructure. This phase forms in the middle of α grains and is large (20-50 μm) [4].

The κ_{ii} and κ_{iii} phases form during the cooling β phase. The κ_{ii} phase is similar to the κ_i phase; however, the crystallites are smaller in diameter (5-10 μm) and not located in the center of the grains of α-phase. This phase is primarily Fe_3Al, but some substitutions for Fe and Al can take place.

The κ_{iii} phase forms from the eutectoid decomposition of β and has an elongated structure [4]. The κ_{iii} phase is primarily NiAl intermetallic, and has the B2 structure. Regions of κ_{iii} and κ_{iii} are located next to one another, since they are both β-phase transforms.

The κ_{iv} phase is another aluminide precipitate formed from cooling of α phase. It is similar in structure to the κ_{ii} phase, and is primarily Fe_3Al intermetallic [4]. Figure 4 shows the microstructure of as-cast NAB.

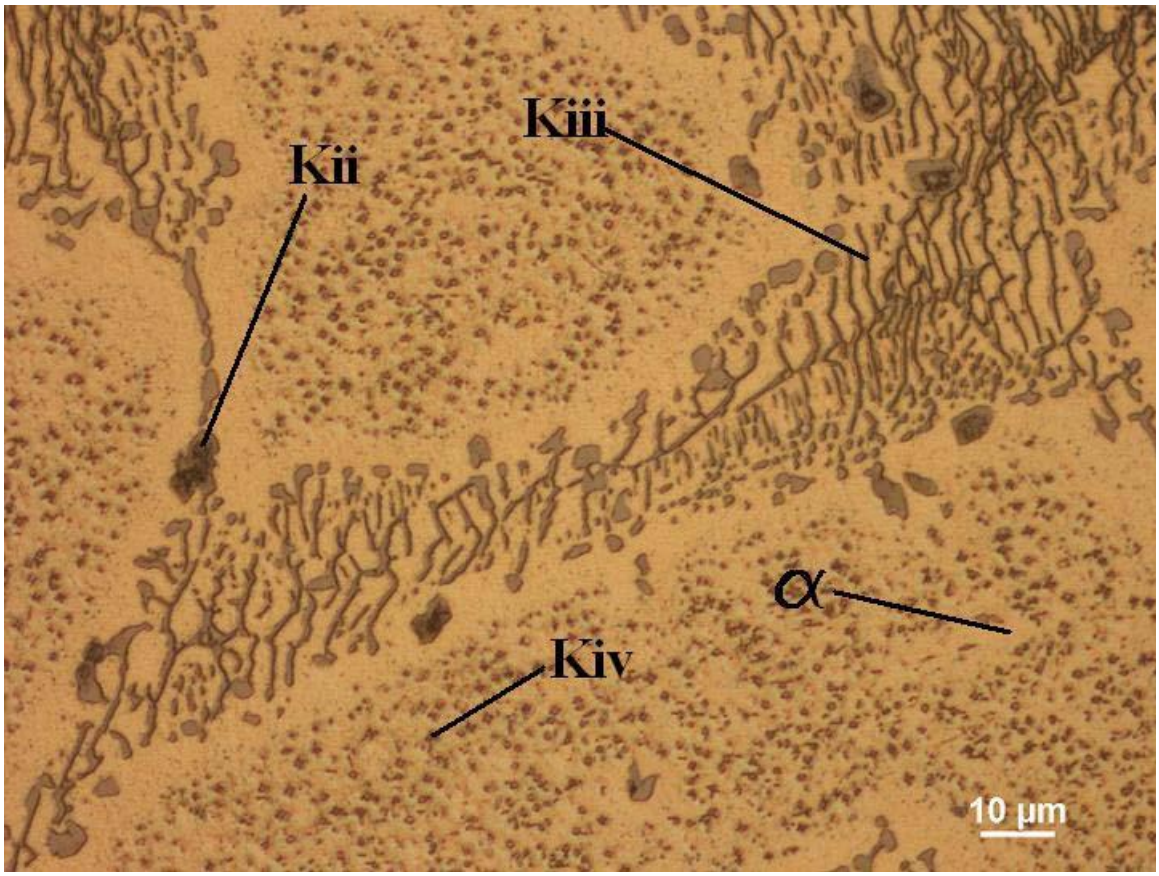

Figure 4. Optical micrograph taken at 50s magnification of as-cast NAB showing α and κ phases (κ_i phase is not present), from [8]

B. NAB AS A PROPELLER MATERIAL

1. Desirable Properties

Nickel Aluminum Bronze is used as a propeller material because it has good mechanical strength, ductility, fracture toughness and corrosion resistance [4]. As a general trend, the higher the aluminum content, the better the corrosion resistance.

2. Limitations of Manufacturing and Repair

Because propellers are cast, the NAB propeller loses some of the more desirable traits that are exhibited in the wrought manufacturing. The castings are several meters in

diameter and several millimeters thick, which results in varying cooling rates and microstructure. These cooling rates can cause high porosity and a course microstructure. The porosity on the surface must be repaired before the propeller can be placed into service, or it will be more prone to cavitation and a decreased service life.

Cavitation damage of a metal's surface occurs when vapor bubbles form and collapse due to intense localized reductions in hydrodynamic pressure [10]. The bubbles then collapse and create a shock that exceeds the elastic limit of the material, breaking its protective films and providing a nucleation site for subsequent nucleation of bubbles.

In order to combat cavitation damage of Nickel Aluminum Bronze (NAB) propellers, refinement of the grain structure using friction stir processing (FSP) has been proposed. The castings of NAB are very large and have low cooling rates. According to McNelley, FSP results in closure of porosity and contributes to improved mechanical properties [11].

C. FRICTION STIR WELDING AND PROCESSING

Friction Stir Processing (FSP) is derived from Friction Stir Welding (FSW) which was first developed by the Welding Institute (TWI) in Cambridge, England [12]. The process is a solid-state technique that involves forcing a wear-resistant, rotating tool into the surface of the work piece (Figure 5). The tool is then traversed across the piece at a predetermined velocity. The three main parameters that affect the microstructure are tool rotation speed, geometry of the pin and velocity at which the pin travels down the plate [12].

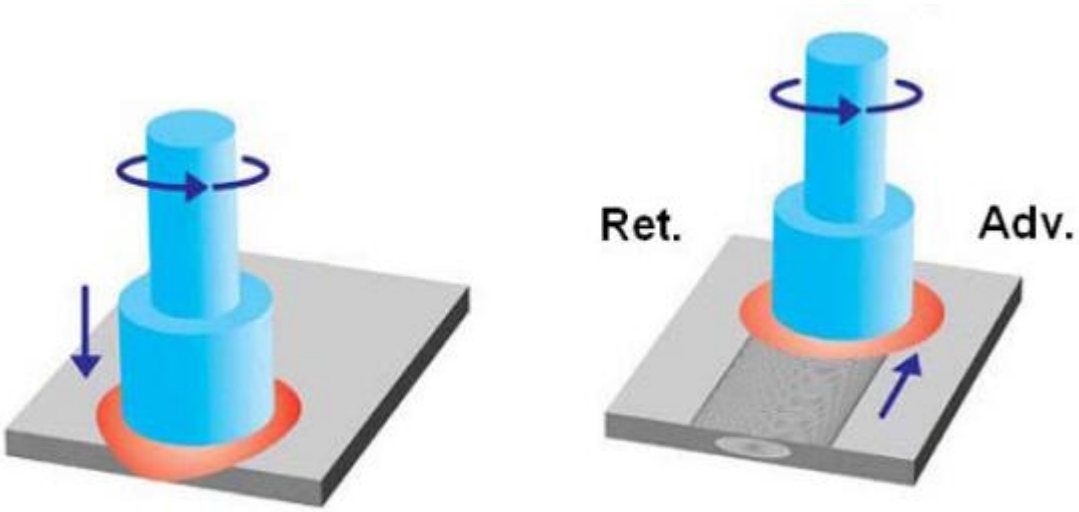

Figure 5. Friction stir processing set up, from [8]

The tool, which is forced into the work-piece, consists of a pin and shoulder and is made of a wear resistant material such as a tungsten alloy. The pin is mounted on a larger diameter pin, or shoulder, which keeps the work-piece metal from moving upward during processing. When the pin and shoulder rotate, the material is plastically deformed [12].

Since FSP is a solid state process, there is no fusion zone; rather, it is replaced by a stir zone (SZ), a small heat affected zone (HAZ) and a thermo-mechanically affected zone (TMAZ). The HAZ and TMAZ lay on the outside of the stir zone. A transverse section of a FSP weld is shown in Figure 6.

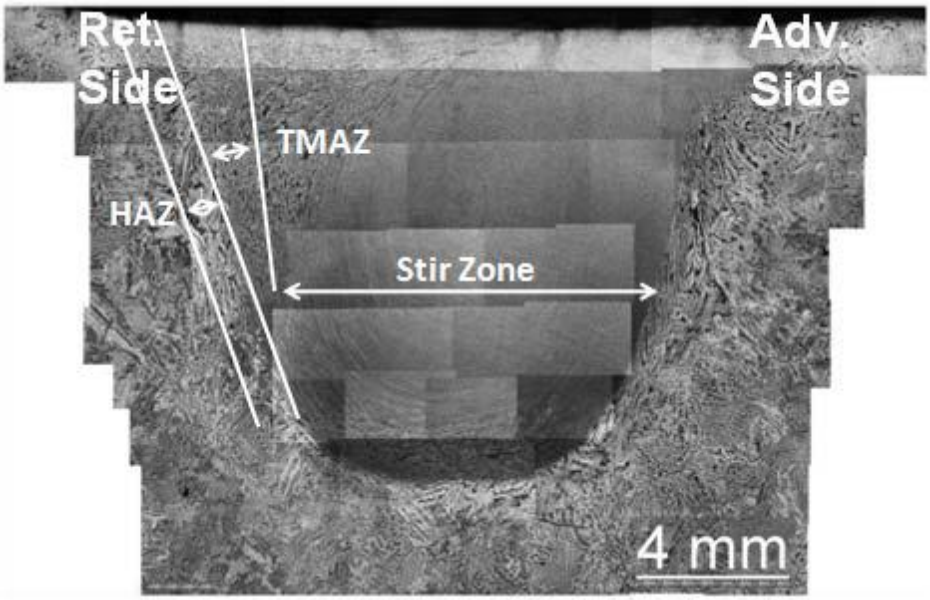

Figure 6. Transverse view of friction stir processed NAB, from [8]

This composite image was taken such that the direction of pin travel was into the page; hence, the advancing side of the microstructure is on the right and the retreating side is on the left.

In the SZ, severe deformation and large gradients in strain and temperature occur. The combination of these three factors leads to refinement and homogenization of the microstructure, which in turn improves the strength and ductility of the material [11].

FSP NAB improves select mechanical properties. For example, yield strength, tensile strength, fatigue life increase by more than 100, 60 and 100 percent, respectively, while maintaining the strain-to-failure at a level in excess of 10 percent [11].

Whether FSP improves corrosion resistance for NAB is not clear. Previous corrosion studies show that selective phase corrosion (SPC) occurs in Nickel Aluminum Bronze [13]. According to Lenard et all, small variations in the heat treatment of NAB have a marked effect on the microstructure and the corrosion resistance [13]. FSP adds heat into the work-piece and refines the microstructure. While the specimen in the Lenard experiments had a retained β' phase which rapidly underwent SPC, they also state

that NAB without this phase present would eventually undergo SPC. Previous microstructural analysis for the FSP NAB in this study has revealed an absence of the retained β' phase.

D. OBJECTIVES FOR THIS THESIS RESEARCH

This thesis will test two hypotheses: 1.) that FSP will improve the corrosion resistance of NAB and 2.) that each specific phase in the FSP microstructure will have its own passivation characteristics. The NAB used for this study had no retained β' phase; however, it is hypothesized that the microstructure refinement created by FSP improves NAB's corrosion resistance and that each specific phase of NAB exhibits its own unique passive film. In order for FSP to be considered as a method of surface processing and repair for the USN, it must still retain its good corrosion resistance. To test the change in corrosion resistance, a variety of tests, including cyclic polarization and electrochemical impedance spectroscopy, were run.

E. EXPERIMENTAL METHODS BACKGROUND

1. Cyclic Polarization

Cyclic polarization (CP) is an experimental method where passive film stability, as a function of potential can be explored. CP essentially takes a vertical slice (constant pH) through the Pourbaix [14]. During a cyclic polarization scan a gradually increasing potential is applied to the test specimen. The potential applied is relative to the open circuit corrosion potential (OCP or E_{corr}), which is defined as the point where the current densities for all anodic and cathodic reactions occurring on the surface of the corroding specimen are equal [10] (Figure 7).

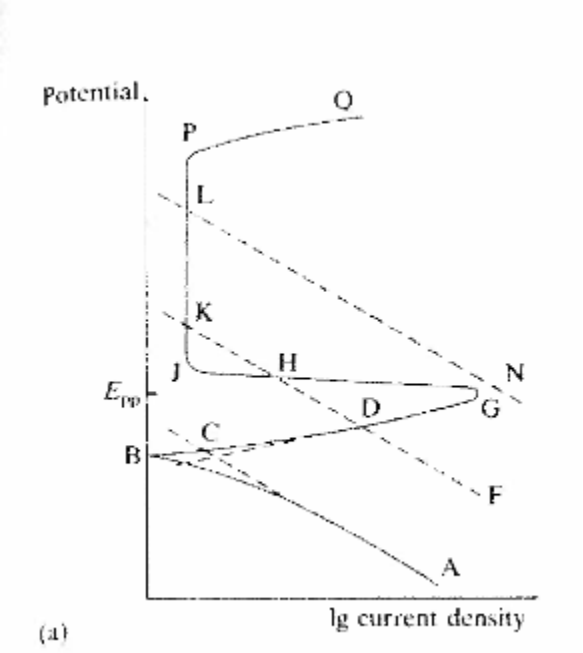

Figure 7. Cyclic polarization of passivating material OCP is shown as point B, from [10]

The OCP also coincides with the intersection of the anodic (line DB) and cathodic (line AB) Tafel lines. The test begins by applying a potential to the specimen that is more negative or more cathodic than the OCP. The voltage is then increased until it reaches the OCP (B). The test then proceeds to potential levels more anodic than the OCP ($E > E_{OCP}$). After the open circuit corrosion potential has been surpassed, the specimen may undergo general or localized corrosion, depending upon the amount of potential difference between the applied and open circuit potential values. Application of the potential may allow a passive film to be formed, which in turn slows down the corrosion rate until the passivation potential (G) is reached. The growth of the film corresponds with a decrease in the corrosion current density (line GJ) and a passivation zone (line JP), where current density remains low until the film breaks down. Spontaneous breakdown of the passive film and localized corrosion require that the applied potential exceed the critical potential [15]:

$$E_{corr} > E_{criti} \quad (1)$$

Above this potential, pits form and the current density again rises (line PQ). The anodic scan continues until either the apex voltage or the apex current density (Q), both set by the user, is reached. Once either the apex current or voltage is reached, a reverse scan, in which the voltage is decreased, begins.

During the reverse scan, the damaged film can repassivate by repairing itself [10]. Based upon the area formed by this hysteresis loop, the ability of the film to repassivate can be determined. The smaller the area, the more easily the film repassivates. The more easily a film repassivates, the less susceptible it is to pitting as the active sites are covered by the reforming surface. Once the applied voltage is back to the OCP, the scan is completed.

2. Electrochemical Impedance and Surface Modeling

The surface of the as-cast and friction-stirred NAB consists of electrochemically active sites corresponding to the α, β, κ_{ii}, κ_{iii}, and κ_{iv} phases. Each type of site has a unique activity and a corresponding electrochemical admittance (inverse of impedance). The overall complex admittance of the exposed surface, Y_{total}, consists of a parallel combination of the complex admittances for the individual sites, Y_α, Y_β, $Y_{\kappa ii}$, $Y_{\kappa iii}$, $Y_{\kappa iv}$, and Y_z:

$$Y_{total} = x_\alpha Y_\alpha + x_\beta Y_\beta + x_{\kappa ii} Y_{\kappa ii} + x_{\kappa iii} Y_{\kappa iii} + x_{\kappa iv} Y_{\kappa iv} + x_z Y_z \quad (2)$$

The complex admittance is formed from its respective real and imaginary parts [16]:

$$Y_{total} = Y_{total} + jY_{tot} \quad (3)$$

Note the inverse relationship between Y_{total} and Z_{total}:

$$Z_{total} = Y_{tot}^{-1} \quad (4)$$

Similarly, the complex impedance is also formed from its respective real and imaginary parts:

$$Z_{total} = Z_{total} + jZ_{tot}$$ (5)

The coefficients x_α, x_β, $x_{\kappa ii}$, $x_{\kappa iii}$, and $x_{\kappa iv}$, are the fractions of the exposed surface occupied by the indicated crystalline phases, and the sum of the area fractions is unity [16]:

$$x_\alpha + x_\beta + x_{\kappa ii} + x_{\kappa iii} + x_{\kappa iv} = 1$$ (6)

FSP changes the distribution of surface phases, thereby changing the values of x_α, x_β, $x_{\kappa ii}$, $x_{\kappa iii}$, and $x_{\kappa iv}$ and the value of the overall admittance, Y_{total}.

The characteristic admittance for each type of active area on the surface is potential dependent; thus, some sites readily oxidize to form thick passive films, while other sites remain either immune or electrochemically active resulting from each surface area being covered with a unique oxide phase that is dependent upon the elemental composition of the underlying grain.

The kinetics of a corroding specimen can be studied using electrochemical impedance spectroscopy (EIS). In EIS, the specimen produces a current response to an alternating potential signal. A small-amplitude sinusoidal voltage modulation (e) is applied between the reference and working electrode and a corresponding current response, i, flows between the counter and working electrodes. As discussed by Bard and Falkner [15]:

$$e = E\sin(\omega t))$$ (7)

$$i = I\sin(\omega t + \phi)$$ (8)

The voltage modulation (e) and current response (i) can also be represented in phasor notation as (E) and (I). The voltage modulation and current response are than

related through the complex impedance $\angle$:

$$E\_IZ \tag{9}$$

The complex impedance consists of real and imaginary parts, which are used to define the phase angle between the potential and current, as well as the magnitude of the impedance:

$$Z(\omega) = Z_r(\omega) + j Z_j(\omega) \tag{10}$$

The complex impedance, both its real and imaginary parts, is frequency dependent. From simple geometric arguments, the phase angle, the arctangent of the ratio of the imaginary to the real part of the complex impedance, can be determined [15]:

$$\phi(\omega) = \arctan\left(\frac{Z_j(\omega)}{Z_r(\omega)}\right) \tag{11}$$

Similarly, the amplitude is defined as:

$$|Z(\omega)| = \sqrt{Z_r^2(\omega) + Z_j^2(\omega)} \tag{12}$$

Conversely, the real and imaginary parts can also be defined in terms of the phase and amplitude of the complex impedance.

$$Z_j(\omega) = |Z(\omega)| \sin(\phi(\omega)) \tag{13}$$

$$Z_r(\omega) = |Z(\omega)| \cos(\phi(\omega)) \tag{14}$$

The frequency response of the impedance can also be represented as:

$$Z(\omega) = Z_o \frac{sin(\omega t)}{\sin(\omega t + \phi)} \tag{15}$$

Where

$$\omega = 2\pi f \tag{16}$$

and where f is the frequency applied in Hertz [15].

The real and imaginary portions of the impedance can be represented by a Nyquist plot which shows a specific impedance value for a specific frequency; however, no values of frequency are shown as only the real and imaginary impedance values are plotted on the x and y axis, respectively. A Nyquist semi-circle represents one time constant as shown in Figure 8; however, due to the complex nature of most systems, many semicircles are usually present. Many time constants may be required for properly characterizing a complex system such as NAB [16].

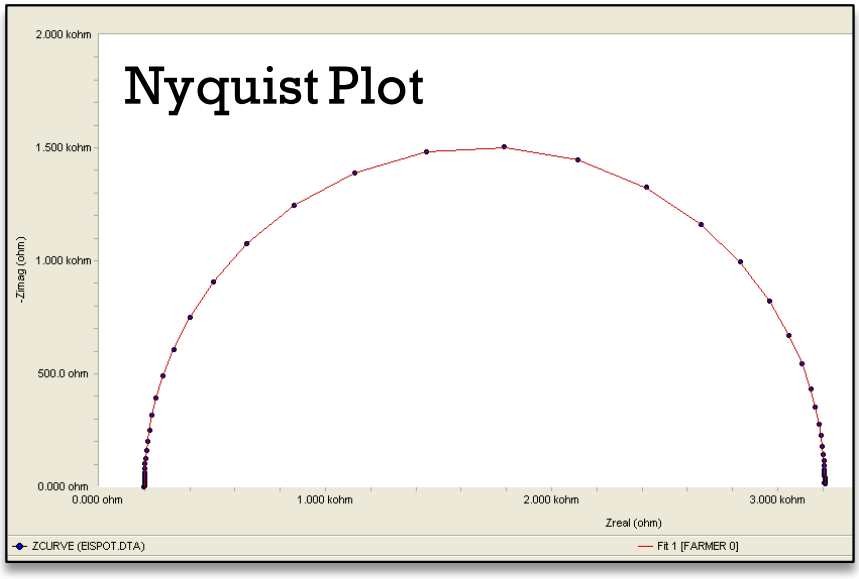

Figure 8. The Nyiquist plot for the equivalent circuit shown in Figure 12. A larger format version of this Figure is at the end of this thesis in the Appendix.

In order to connect the impedance to the applied frequency, a different plot, or Bode Plot, is needed. In a Bode plot, the log of the absolute values of impedance is plotted verse frequency as shown in Figure 9.

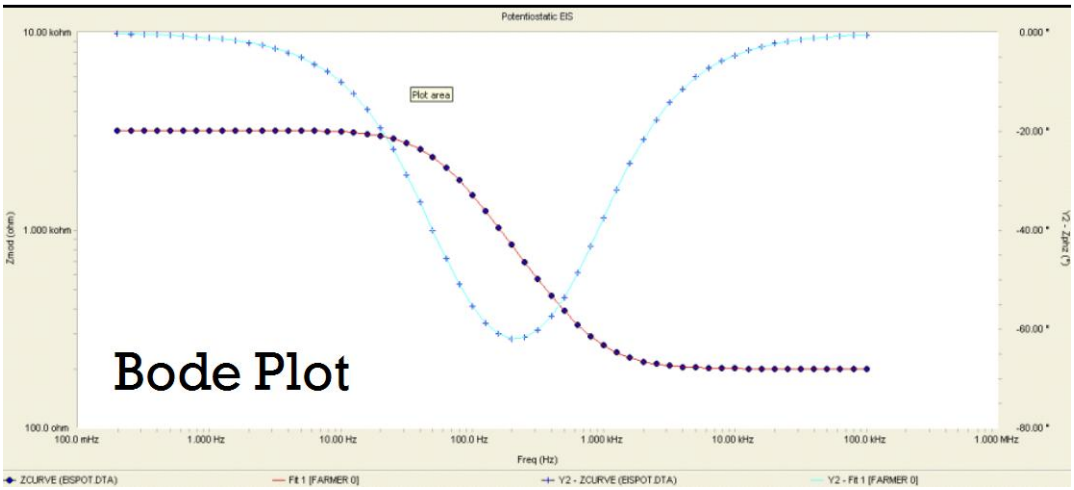

Figure 9. Bode plot for the equivalent circuit shown in Figure 12. A larger format version of this Figure is at the end of this thesis in the Appendix.

To give the data in the Nyquist and Bode plots physical significance, an electrical circuit model is constructed using resistors, capacitors and inductors. The resistor has entirely real impedance, while the latter two have a purely imaginary response. Table 2 shows the most common electrical circuit elements, their current verse voltage relationship and as their impedance response to frequency.

Table 2. Common electrical circuit elements, from [16]

Component	Current vs. Voltage	Impedance
Resistor	E=IR	Z = R
Inductor	E=L di/dt	Z= jωL
Capacitor	I= C dE/dt	Z = 1/jωC

The impedances of each element can then be added using standard impedance mathematics. For instance, impedances in series as shown in Figure 10 can be added to calculate the total resistance:

$$Z_t = Z_1 + Z_2 + Z_3 \quad (17)$$

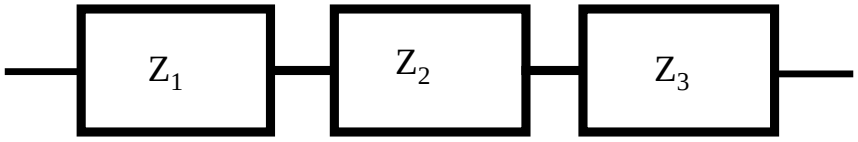

Figure 10. Series Impedance

For impedances in parallel as shown in Figure 11, the total impedance is calculated as follows:

$$Z_T = \frac{1}{z_1} + \frac{1}{z_2} + \frac{1}{z_3} \quad (18)$$

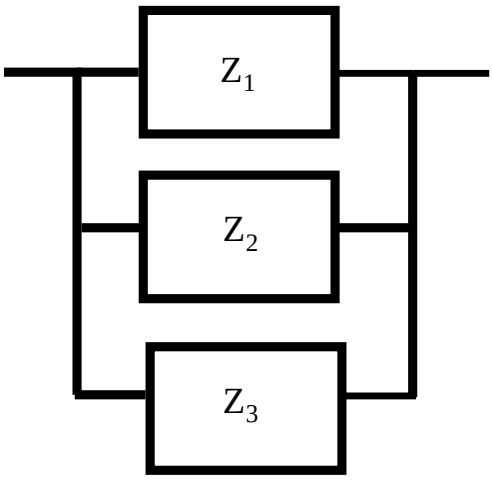

Figure 11. Parallel Impedances

Using these basic elements, models to describe the basic chemical and kinetic reactions of the cell can be accounted for. These include, but are not limited to the following: solution resistance, mass transport, chemical reaction, double layer capacitance, and porous film layer and are described in further detail in the subsequent paragraphs.

3. Basic Circuit Elements and Considerations

a. Solution Resistance, R_S

The solution resistance, R_s, is the resistance between the working and reference electrodes in the cell due to the electrolyte and is calculated using equation 19 where ρ is the solution resistivity, l is length and A is the bound area.

$$R_S = \rho \frac{l}{A} \tag{19}$$

b. Double Layer Capacitance

A double layer forms on between the surface of the specimen and the electrolyte when ions stick to the surface of the specimen. This forms a small capacitor whose value is dependent upon ion concentration, ion type, oxide layer composition, electrode roughness and impurity adsorption [16]. Expected values for double layer capacitance are expected to be between 20 and 60 microfarads for each 1 cm^2 of electrode area. [16].

c. Polarization Resistance, R_P

The next element that must be considered is the polarization resistance of the cell. This resistance arises by forcing the electrode away from its open circuit potential (OCP). The OCP is defined as the potential at which the anodic and cathodic current densities are equal. The amount of resistance depends on the rate of reaction at the surface of the electrode. The amount of current, which is proportional to the reaction rate, is controlled by the diffusion of reactants to and away from the electrode and is given by equation 20 where, I is the measured cell current, I_{corr} is the corrosion current, E_{oc} is the open circuit potential, β_a is the anodic Beta coefficient and β_c is the cathodic Beta coefficient.

$$I = I_{corr}\left(e^{\frac{2.303(E-E_{OC})}{\beta a}} - e^{\frac{-2.303(E-E_{OC})}{\beta c}}\right) \quad (20)$$

This element behaves like a resistor when small signals are applied, making I_{corr} related to R_P , where R_P is the polarization resistance as given in Equation 21 [16].

$$I_{corr} = \frac{\beta_a \beta_c}{2.303(\beta_a + \beta_c)} * \left(\frac{1}{R_p}\right) \quad (21)$$

The polarization resistance is a function of kinetics.

d. Charge Transfer Resistance, R_{ct}

The transfer of charge due to the kinetics of equation x produces another resistive element in the circuit: the charge transfer resistance, R_{ct} [16]:

$$Me \Leftrightarrow Me^{n+} + ne^{-} \quad (22)$$

In this reaction, metal ions are dissolved into the electrolyte and electrons from the electrolyte enter into the metal [16]. The speed of the dissolution is governed by the type of reaction it is, the temperature and the concentration of the products and potential in the cell. This relationship is simplified and related to the Butler Volmer equation, which results in [16]:

$$R_{ct} = \frac{RT}{nF i_O} \quad (23)$$

e. Diffusion

In addition to the charge transfer resistance, the diffusion adds another element, Warburg Impedance (W), to the circuit. Warburg impedance varies with the

frequency. When the frequency is high, the reactants do not have to diffuse very far; thus, the impedance is low, while at high frequencies, the reactants must diffuse further, which increases the impedance. In the analysis provided, a finite thickness was assumed; therefore, the impedance is [16]

$$Z_o = \sigma \omega^{-1/2}(1-j)\tanh\left(\delta\left(\frac{j\omega}{D}\right)^{1/2}\right) \tag{24}$$

where σ is the Warburg coefficient, D is the average value of the diffusion coefficients of the diffusing species, and δ is the nernst diffusion layer thickness.

A sample circuit with one time constant is shown in Figure 12. Figure 12 corresponds with the Nyquist and Bode plots, Figures 10 and 11, respectively.

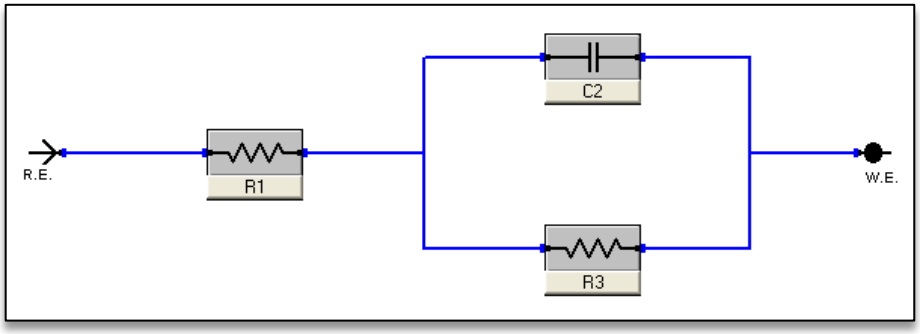

Figure 12. Simple electric circuit model

III. EXPERIMENTAL PROCEDURE

A. OVERVIEW

This study focuses on the passive film formation of nickel aluminum bronze in the as-cast (AC) and FSP conditions. This was accomplished by using cyclic polarization (CP) and electrochemical impedance spectroscopy (EIS) scans. The results were then modeled using electric circuit comparisons. In addition, scanning electron microscope (SEM) and focused ion beam (FIB) techniques were used to link the microstructure with the formation of the passive films.

B. MATERIAL PROCESSING

A plate of NAB was FSP by Rockwell Scientific Corporation (now the Teledyne Scientific Company). The plate was subject to a single pass friction stir at 1200 rotations per minute (RPM) and a traverse rate of 2 inches per minute (IPM). The pass was made using a step spiral densimet tool with a pin depth of 12.7 mm. The pass created a processing zone with a depth of ½ inch from the as-cast to FSP zones, as shown in Figure 13. The NAB plate was then cut using a Charmilles Andrew EF630 electric discharge machine with at wire diameter of 0.30 mm into seven samples, shown in Figure 13.

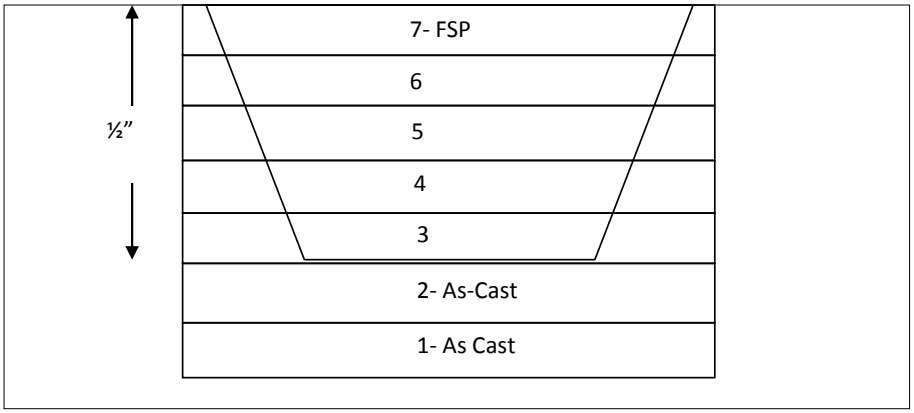

Figure 13. Transverse NAB section showing sample locations

C. SAMPLE PREPARATION

After the samples were sectioned, they were ground and polished. The grinding of the sample was performed using a Buehler ECOMET variable speed grinder-polisher with a succession of sandpapers: 400, 1200, 2400, and 4000 grit. After each paper level, the sample was rinsed with water. Next the samples were polished using an ECOMET 3 Variable Speed Grinder-Polisher with a 3µm diamond suspension followed by a 1µm diamond suspension until a mirror finish free of scratches was obtained. Post-polishing the samples were drenched with methanol and blasted with hot air to keep the mirror finish. This procedure was repeated after each EIS sequence in order to remove the passive films formed during the experiments and to provide a clean surface for the next test.

D. CORROSION TESTING

1. Setup

The CP and EIS corrosion tests were conducted in a closed system, standard three electrode cell, shown in Figure 14, which consists of a working electrode, a graphite counter-electrode and a standard hydrogen reference electrode.

All tests were conducted in Monterey Bay seawater at 30 or 90 degrees celcius. The cell temperature was regulated using a closed system of water heaters and coolers set to the desired testing temperature of 30 or 90 ˚C. The cell was de-aerated using nitrogen gas and had a positive pressure to ensure no gas aside from the nitrogen was allowed into the system.

Round disc specimen were used in all tests. The area exposed to electrolyte for all tests was 0.931 cm^2.

Figure 14. Standard three-cell test apparatus

2. Cyclic Polarization

The CP scans were conducted in the three electrode cell at 30 degrees using the Gamry Echem Framework software. The test began with a 60 second conditioning time, followed by a 60 second delay. The scan rate for the test was 1mV/s in the forward and reverse directions, with an apex current of 10 $mA/cm^2$and apex and final voltages of 1.5 V and 0 V, respectively.

3. Electrochemical Impedance Spectroscopy

The EIS tests were conducted in the three electrode cell. Table 3 shows the series of procedures run on each of the samples.

Table 3. Electrochemical impedance spectroscopy scans and film formation procedures

Test	Voltage Applied (mV)	Time Applied (s)	Conditioning Time (s)	Delay Time (s)	Initial frequency (Hz)	Final Frequency (Hz)
Initial EIS	0	---------	900	60	300,000	0.01
Film Formation	100	900	-------	---------	---------	----------
Post Film Formation EIS	0	----------	900	60	300,000	0.01
Second Film Formation	100	900	---------	------	---------	----------
Post 2nd FF EIS	0	---------	0	60	300,000	0.01
Post 2nd FF EIS (100 mV)	100	----------	0	60	300,000	0.01

The first EIS scan was conducted prior to any film formation with no applied voltage and a conditioning time of 900 seconds was run with an initial frequency of $3*10^5$ Hz and a final frequency of 0.01 Hz. It was followed by a potentiostatic test, or film formation run, of 100 mV for 900 seconds. Next, another EIS scan identical to the first EIS scan was performed. A second film formation of 100 mV for 900 seconds was conducted. Again, an EIS scan was run; however, no conditioning time was allotted. This EIS scan was finally followed by the last EIS scan which applied a 100 mV potential with no conditioning time.

E. MODELING

The EIS data collected above was then analyzed using Gamry Echem Analyst software. A simple Randle's circuit, as shown in Figure 12, was initially constructed to model the EIS data. Due to the complexity of the NAB and the hypothesis that each

phase forms its own distinct passive film, a more developed model was required. The circuit elements discussed in detail in the background section were used to create the model shown in Figure 15. This model has three time constants and fits a majority of the EIS scans. Its relevance is discussed further in the results section.

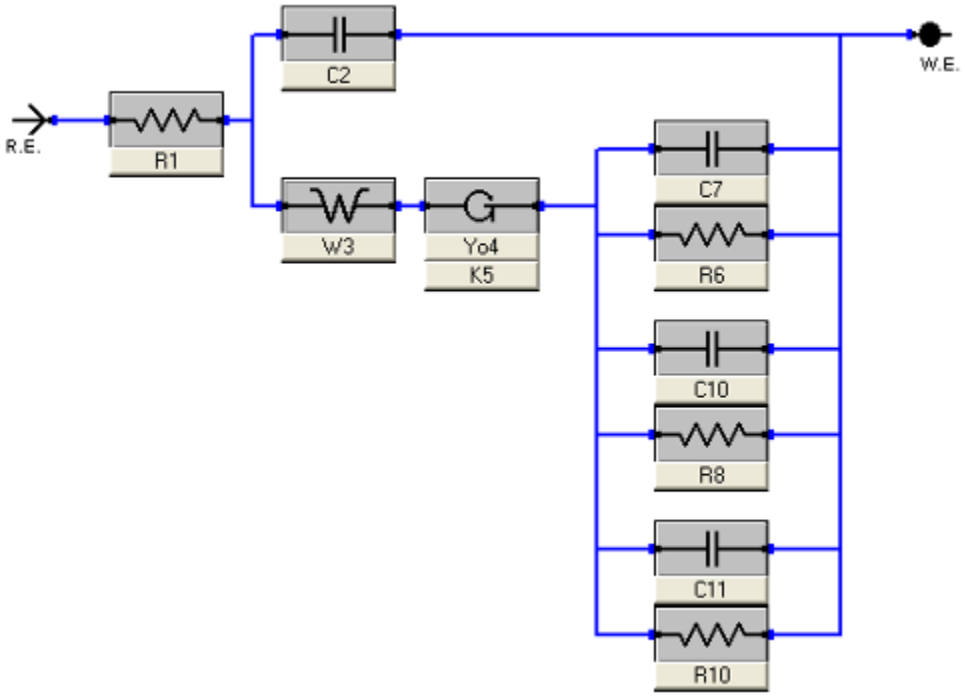

Figure 15. Electric circuit model for NAB passive film, three RC circuit

F. MICROSCOPY

After corrosion testing, the samples were mounted and imaged using the Zeiss Neon 40 Smart SEM V05.03 Field Emission Scanning Electron Microscope. Images of the surface were taken both pre- and post corrosion test at 20 keV. With SEM micrographs, the passive films formed on the surface of the NAB were linked with the underlying microstructure. Using this technique, the hypothesis that each crystalline phase has its own unique passive film was supported.

THIS PAGE INTENTIONALLY LEFT BLANK

IV. RESULTS AND DISCUSSION

A. OVERVIEW

Six samples of NAB processed with FSP at 1200 RPM and 2 IPM were studied. The samples ranged from the top of the processing zone, Sample 7, to the as-cast (AC) microstructure, Sample 2.

Using CP and EIS, the passive films and corrosion resistance formed on the surfaces of the samples were evaluated. In addition SEM images were used to connect FSP's effect on the microstructure with resulting changes in the passive films.

B. CYCLIC POLARIZATION

In this section the CP data collected at 30˚C will be examined to draw conclusions of the effect of FSP on the passive films formed on the AC and FSP samples. In Figure 16 the as cast sample curve is represented in blue, and the FSP Sample, 7, is represented in red.

The cathodic branch of the CP scan is representative of the reduction reactions that occur during the cathodic portion of the scan. Figure 16 shows a decrease in current level for the FSP sample when compared to the AC Sample 2. A lower cathodic current equates to an increased resistance to undergo reduction reactions; thus, the FSP material is more corrosion resistant than the AC material. It is postulated that this decrease is due to the loss of electro-catalytic sites being swept under the NAB's surface during FSP. In addition to the reduced cathodic current level, the FSP data shows more noise. The noise is attributed to a change in the 3-D surface area of the sites, which have been reduced by grain refinement during FSP.

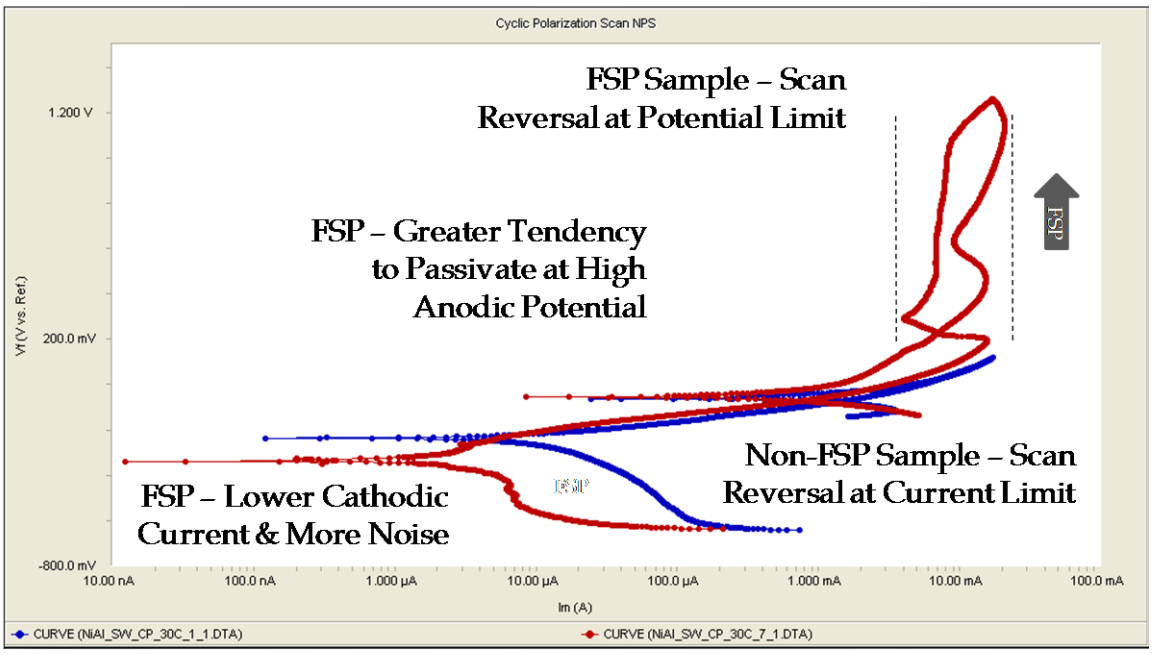

Figure 16. Cyclic polarization overlay of Samples 2 and 7, from [17]. A larger format version of this Figure is at the end of this thesis in the Appendix.

On the anodic side of the potential scan, the Sample 7 shows an increase in stability over a wider range of potential than the AC sample. The AC Sample, 1, never reaches a passivation potential and begins the reverse scan when it reaches a voltage of approximately 0 mV as a result of reaching the scan's current limit of 10 mA/cm^2. Sample 7 shows a passivation zone from 200 mV to 1.2 V. At 1.2 V the scan reaches its potential limit and reverses. The increase in voltage range over which Sample 7 exhibits stability shows that FSP enhances the passive film formation stability of NAB and leads to higher required potentials to break down the film.

C. ELECTROCHEMICAL IMPEDANCE SPECTROSCOPY

This section will discuss electrochemical impedance spectroscopy (EIS), which is a method of investigating passive films formation and corrosion resistance. As in the CP tests, Samples 2, 3, 4, 5, 6, and 7 were tested allowing for the entire range from AC to FSP NAB to be tested. The EIS ran from an ultra high frequency of $3*10^5$ Hz to a very low frequency of 0.01 Hz. Tests were conducted in 30˚C and 90˚C seawater.

Figures 17 and 18 show typical Bode plots, or EIS data, in 30˚C seawater for Samples 2 and 7 respectively that have undergone one film formation run at 100 mV for 900 seconds.

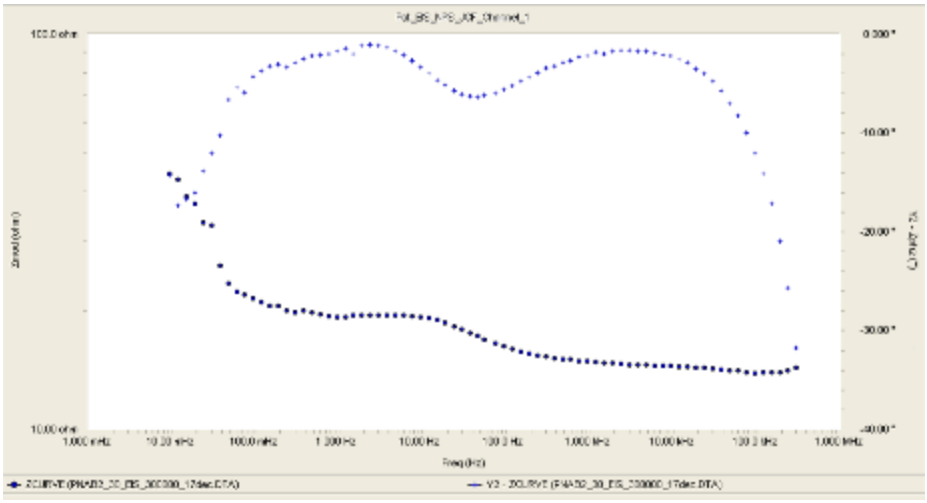

Figure 17. Bode plot for Sample 2 (AC NAB), 30˚C SW. A larger format version of this Figure is at the end of this thesis in the Appendix.

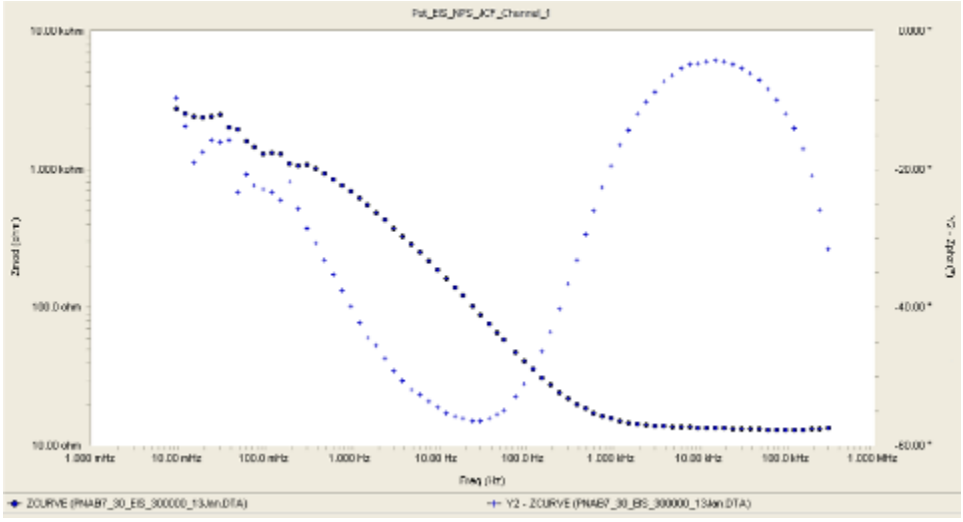

Figure 18. Bode plot for Sample 7 (FSP NAB), 30˚C SW. A larger format version of this Figure is at the end of this thesis in the Appendix.

As seen in the Bode plots, the x-axis shows the frequencies to which the samples were exposed, ranging from ultra high, to ultra low. The left y-axis shows the amplitude data of the EIS test's impedance in ohms, while the right y-axis displays the phase angle data in degrees. By overlaying the Bode plots, as shown in Figure 19, the effect of FSP on NAB can be seen.

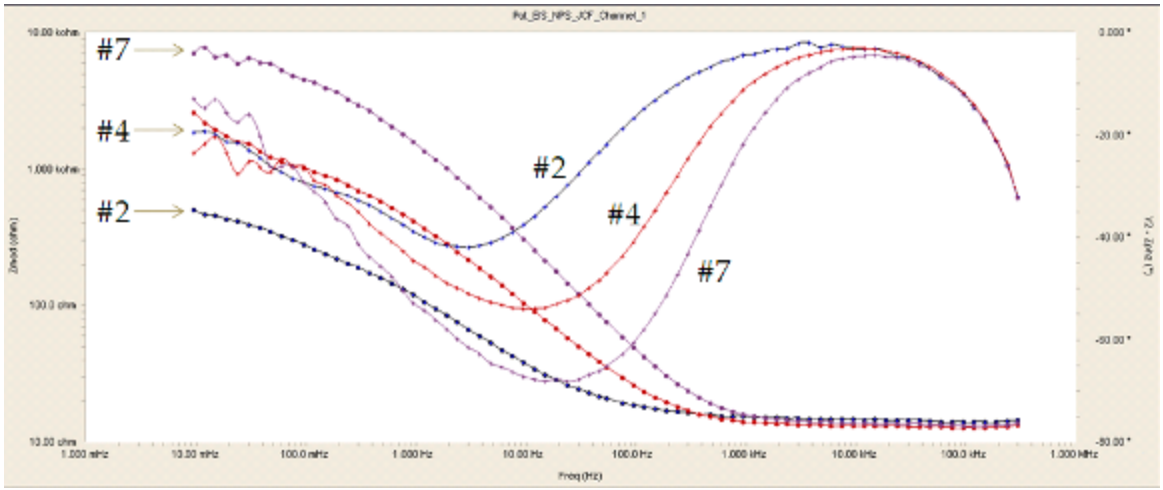

Figure 19. Overlay Bode plot, Samples 2, 4 and 7, 30˚C SW. A larger format version of this Figure is at the end of this thesis in the Appendix.

Figure 19 shows changes in both the phase and amplitude data as the NAB transitions from the AC to FSP condition. At the ultra-high frequencies, around 300 MHz, there is not enough time for ions to diffuse across the passive film, resulting in the solution resistance of the electrolyte being the only impedance present. The impedance values for all samples are approximately the same, which gives the data validity, as all tests were conducted under the same conditions: 30˚C SW. As the frequency moves toward the ultra-low frequencies, the amplitude curves begin to diverge and start to magnify the effect of FSP on the passive films. At the ultra-low frequency of 0.01 Hz, the ions have enough time to interact with the passive film; thus, at this frequency, the change in impedance value can be directly attributed to the effects of FSP. The impedance scale is logarithmic making the increase of Sample 7's impedance that much more remarkable. This increase in impedance shows that the passive film formed on the surface of the FSP material is more passive, has lower corrosion rates and is more stable.

This finding is concurrent with the AC and FSP data from the CP scans, which showed more stable passive films and lower corrosion rates for FSP NAB. Figure 20 shows an annotated version of Figure 19 with the solution resistance being equivalent at the ultra-high frequencies and the passivation resistances and corrosion rates diverging at the ultra-low frequencies. In addition to the increase in passivation resistance, Samples 4 and 7 also show an increase in the amount of noise at these frequencies. Again, the increase in noise is concurrent with the CP data, which showed an increase in the cathodic current noise in the FSP condition.

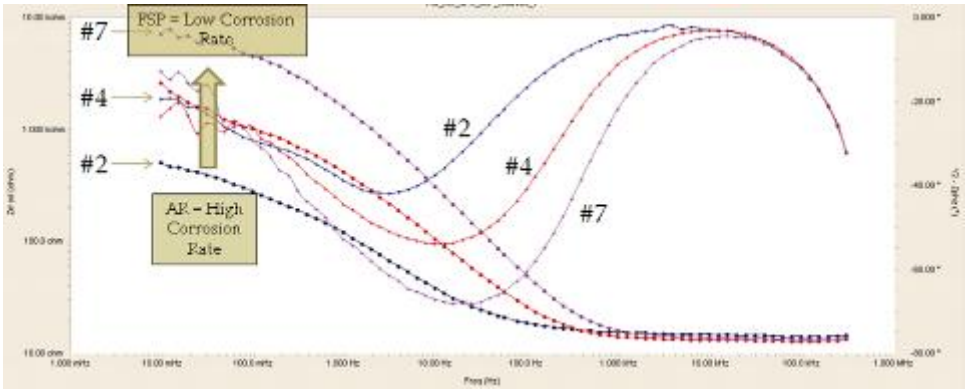

Figure 20. Annotated overlay Bode plot, Samples 2, 4 and 7, 30˚C SW. A larger format version of this Figure is at the end of this thesis in the Appendix.

The EIS tests were also conducted on Samples 2 and 7 at 90˚C. Figure 21 shows an overlay of the Bode plots for this test condition. Note, Sample 7 has undergone a series impedance correction of 35 ohms to correct for a change in electrolyte used. The correction does not affect the overall results at the ultra-low frequency range, as the change in impedance between 2 and 7 is still on the order of three magnitudes.

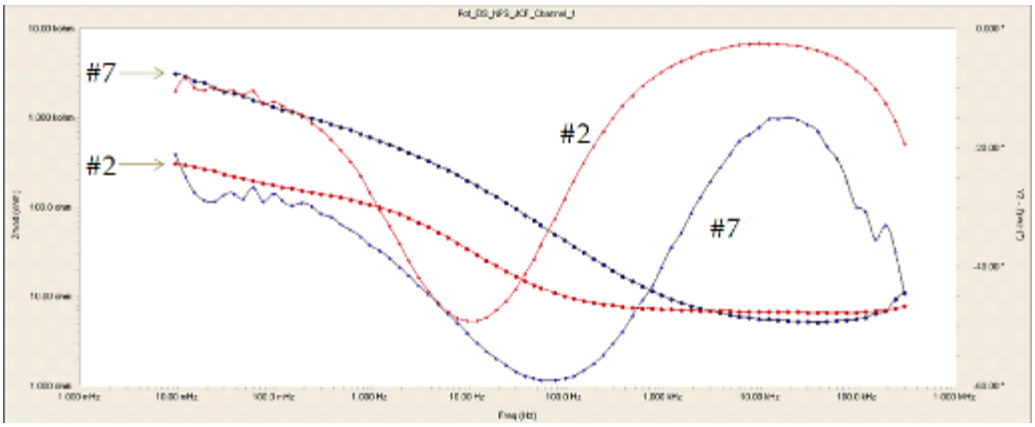

Figure 21. Overlay Bode plot, Samples 2 and 7, 90˚C. A larger format version of this Figure is at the end of this thesis in the Appendix.

D. MODELING

While the qualitative evaluation of the CP and EIS data clearly demonstrate increased corrosion resistance of FSP NAB, quantitative analysis is needed to connect particular changes in the microstructure with the change in overall corrosion response. In order to connect microstructural elements with the EIS data, a multi-component electrical circuit model was constructed. To begin the modeling process, it was hypothesized that each phase of the NAB had its own unique passive film layer as demonstrated in Figure 22.

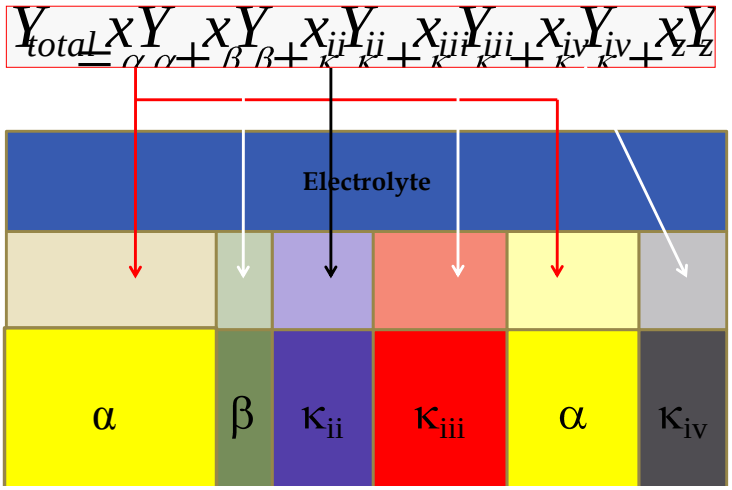

Figure 22. Relationship of crystalline phase and interfacial impedance

The simplest model, model-0 consists of a solution resistance and a single RC circuit, or Randle's circuit (Figure 23).

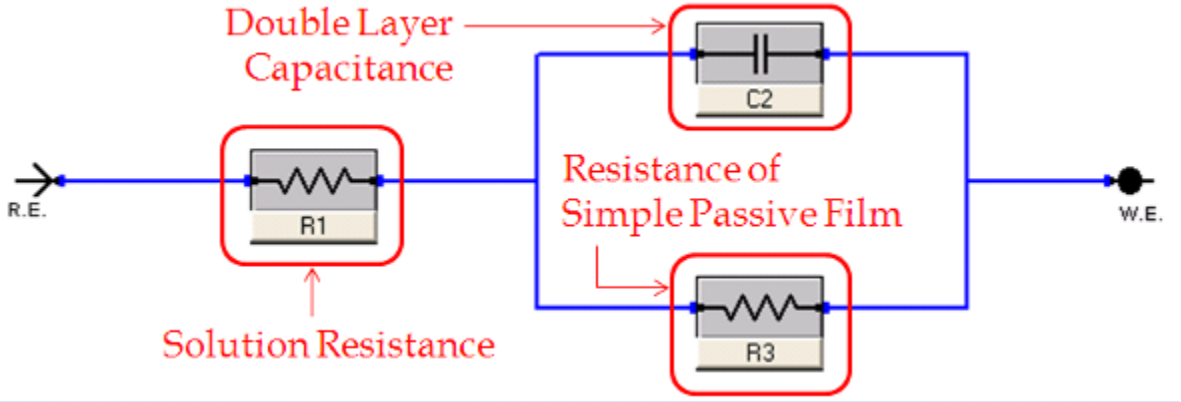

Figure 23. Model-0: single time constant RC network

In this model, the overall passivating film is captured using a capacitor for double layer capacitance and a single resistor for the passivation resistance. Figure 24 shows a physical representation of model-0, with only a single layer of phase independent oxide on the surface.

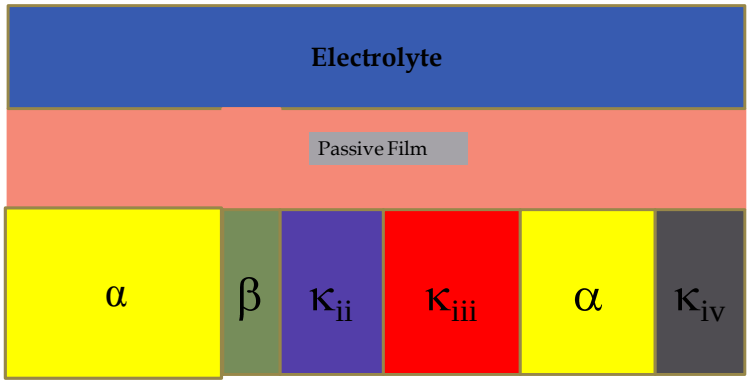

Figure 24. Model-0 physical representation

Due to the simplicity of model-0 compared with the complexity of the real microstructure, the model unsurprisingly did not fit the EIS in amplitude or phase. This disagreement points out that the passivation effects in this material cannot be described as a single passivating film.

In order to include the complexity of the real microstructure, model-15 was constructed (Figure 25). Model-15, like model-0, has a solution resistance and double layer capacitance. In order to account for mass transport and chemical reaction rates of the film, Warburg and Gerisher impedances were added. The final circuit element added was a Bisquert short circuit element which accounts for the impedance of a porous film as a simplified transmission line.

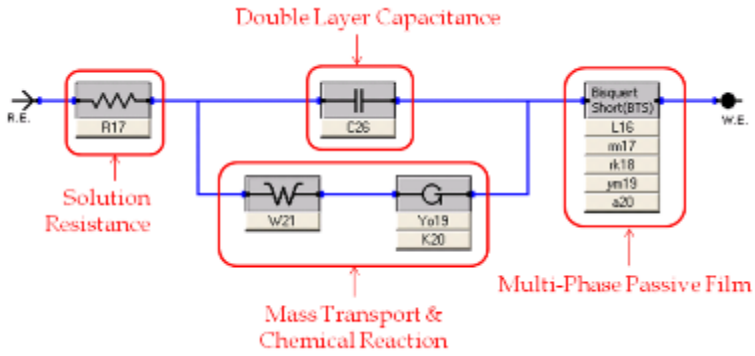

Figure 25. Model-15: Bisquert short circuit

Figure 26 shows the physical representation of the Bisquert short circuit model.

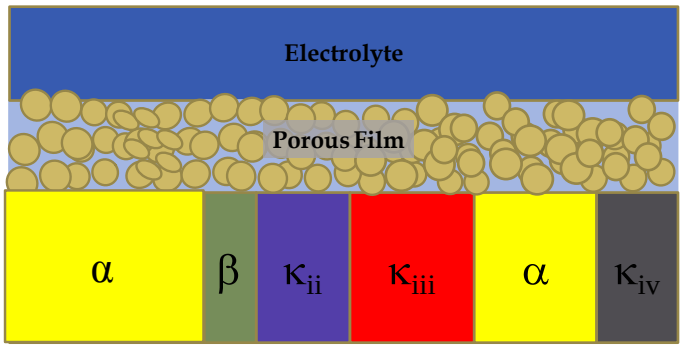

Figure 26. Model-15 physical representation

In Figure 27, the EIS data for Sample 2 (AC) has been fit using both models-0 and 15.

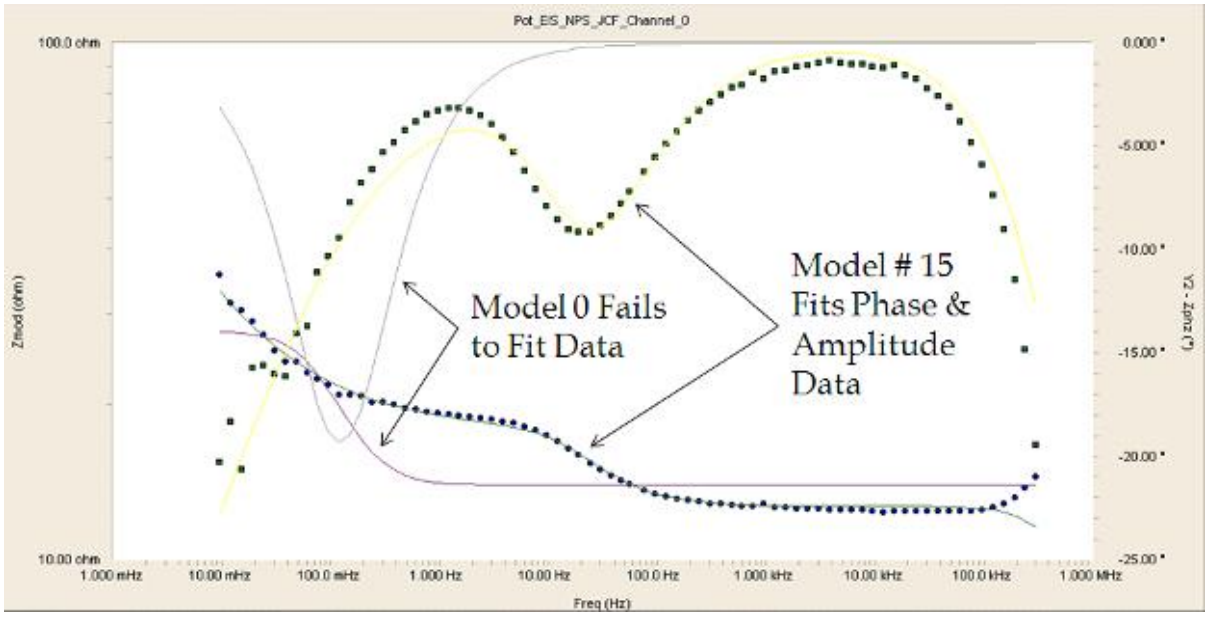

Figure 27. FSP NAB EIS models-0 and 15. A larger format version of this Figure is at the end of this thesis in the Appendix.

As shown, model 0 does not fit the phase or amplitude data; however, model 15 fits both the phase and amplitude data relatively well, with only a small discrepancy at the ultra high frequency. After fitting these two models, model 0 was discarded from further analysis.

In addition to model-15, a model-1, which has a more complex transmission line calculation for the porous film layer, was built. Model-1 replaces the simplified transmission line bisquert short circuit with a unified transmission line, as shown in Figure 28. The major difference between the Bisquert short circuit and the unified transmission line element is the derivation calculation used in the Gamry software [16]. All other circuit elements are the same as in models-0 and15.

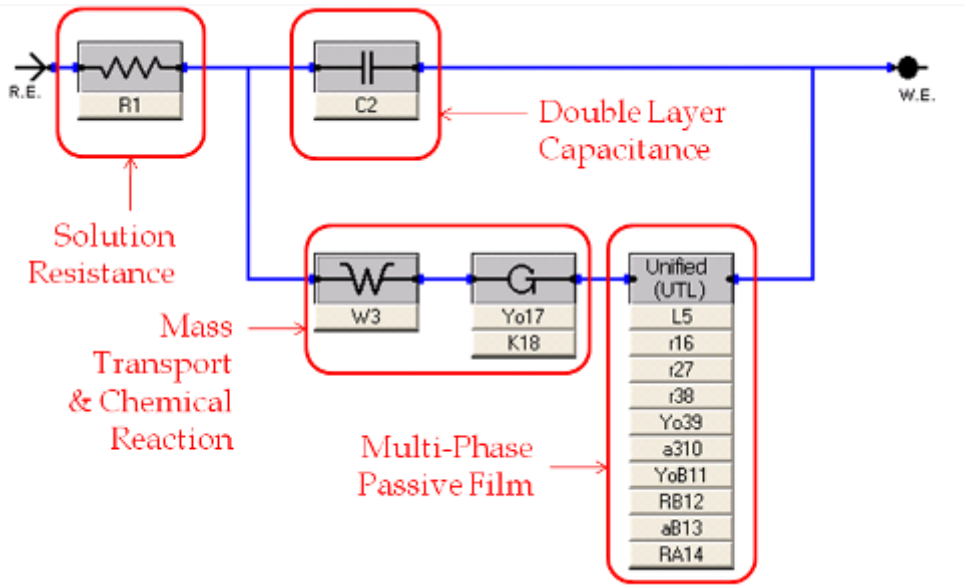

Figure 28. Model-1, unified transmission line.

The physical representation of model-1 is the same as model-15 (Figure 26). Model-1 was then fit to the 30˚C EIS data. Figures 29 and 30 show the model fit to data for Samples 2 and 6, respectively.

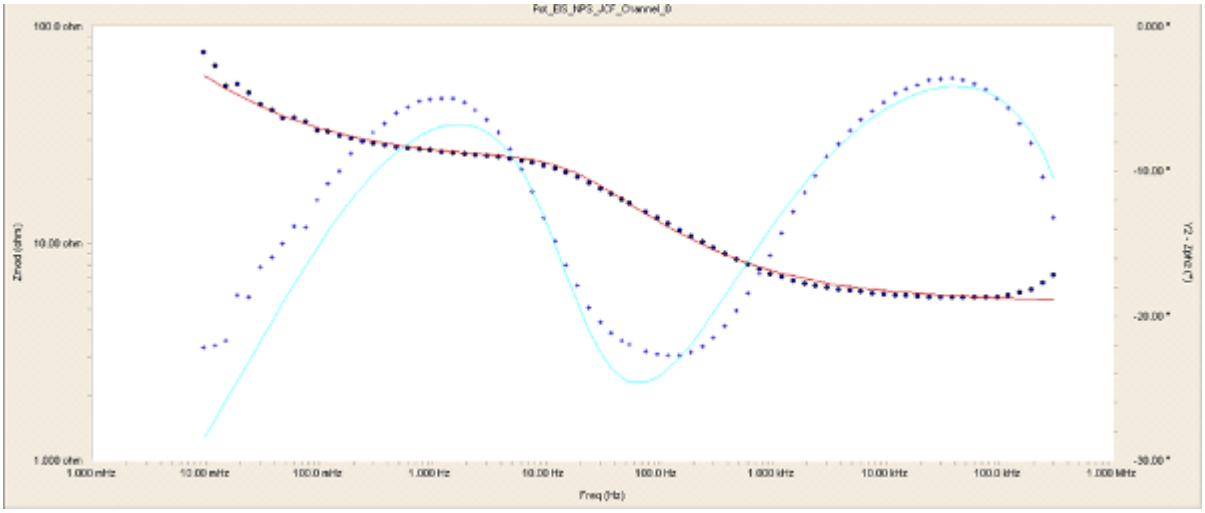

Figure 29. AC (2) NAB SW 30°C model-1 unified transmission line. A larger format version of this Figure is at the end of this thesis in the Appendix.

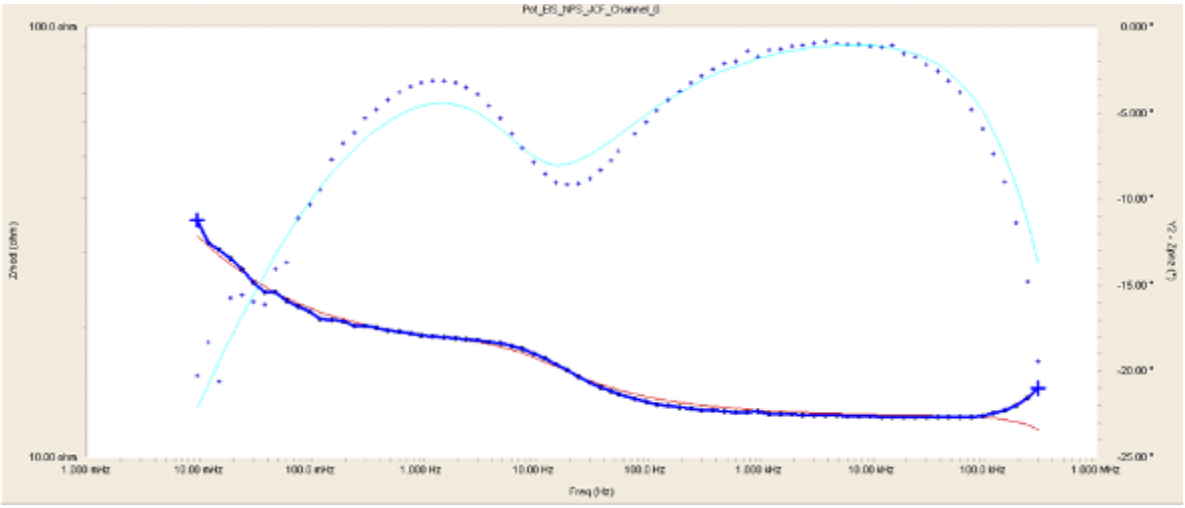

Figure 30. FSP (6) NAB SW 30˚C model-1 unified transmission line. A larger format version of this Figure is at the end of this thesis in the Appendix.

Both Figures 29 and 30 show the good fit of model-1 to both the AC and FSP data. Using excel, a chart comparing the parameters in model-1 over the full range of FSP of NAB, AC (2) to full FSP (7), was constructed and is shown in Figure 31.

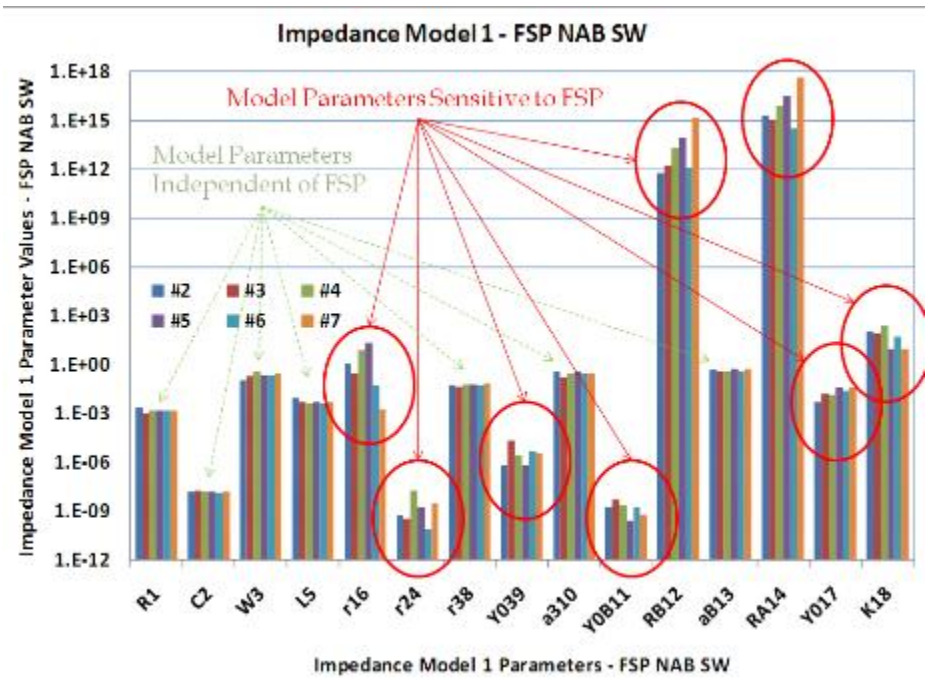

Figure 31. Impedance parameters, model-1

While models-15 and 1 fit the data for all samples, they both lump the impedance of each phase's passive film into one overarching porous film circuit element. To capture the effect of each phase on the passive film, two additional models were constructed. As shown in Figure 32, model-5 consists of three RC circuits in series with one another. Like model's-0 and 15, model-5 still has a solution resistance, double layer capacitance, a Warburg impedance and a gerisher impedance. Figure 33 shows the physical representation of model-5.

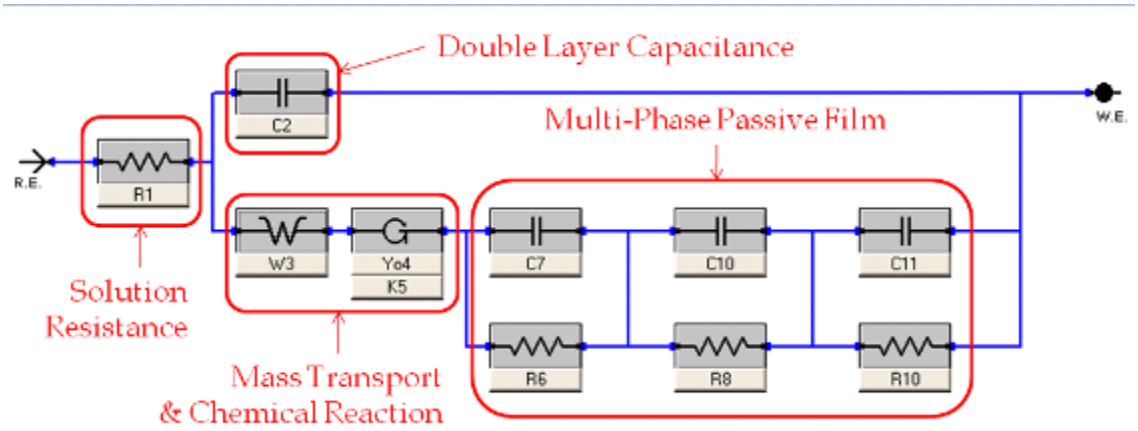

Figure 32. Model-5: three RC series network

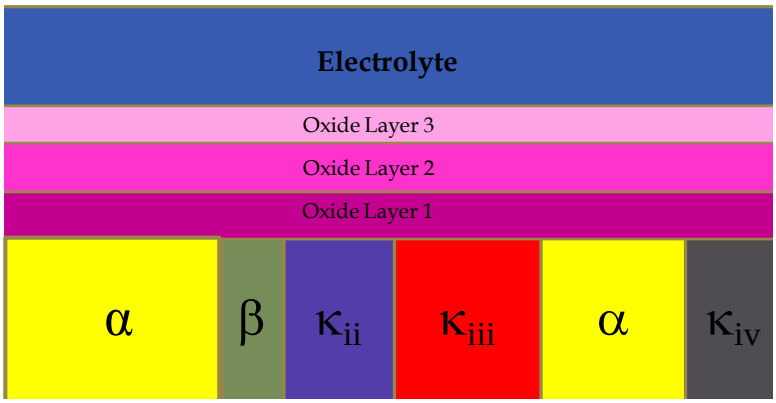

Figure 33. Model-5 physical representation

In order to fit the phase and amplitude data, multiple time constants were required. By placing three RC elements into the circuit model, three time constants were added. Similarly to the previous models-1 and 15, model-5 fits the phase and amplitude

data over the range of frequencies. While each fit seemed to do well initially, when all of the parameters were complied into an excel bar graph, it was noted that the value for R1, the solution resistance changed along with the sample number, suggesting that this parameter changed with FSP; however, all samples were tested in the same sea water at the same temperature and nominal oxygen levels. Thus, the value for R1 should have remained constant despite sample number. The values for the initial fitting of model-5 have been complied and are shown in Figure 34.

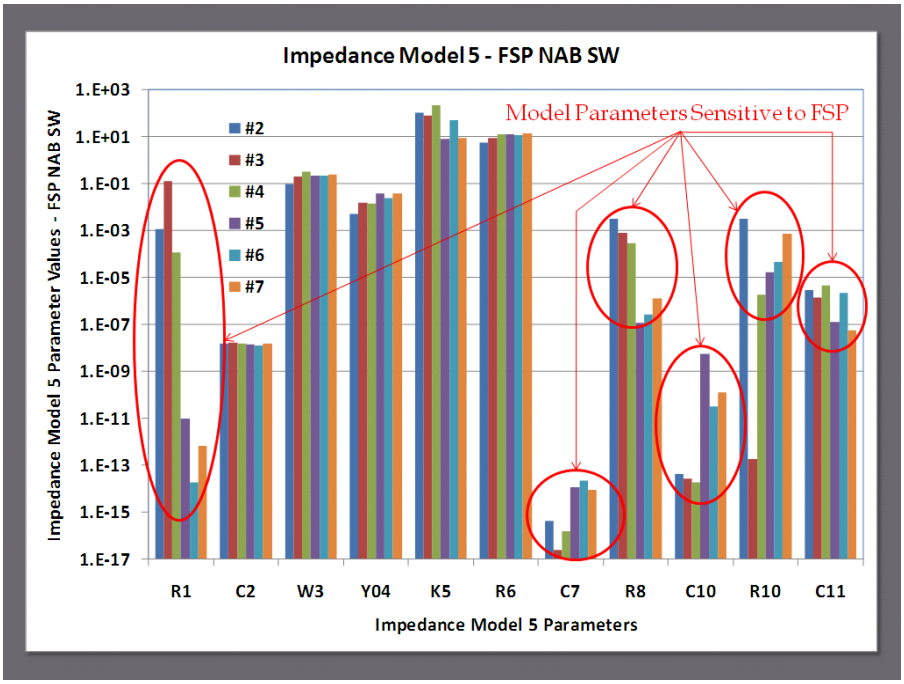

Figure 34. Impedance model-5 – FSP NAB SW

The changing solution resistance pointed out a flaw in the initial guess of the simplex method used to fit the data. As a result, the initial guess for the solution resistance was set closer to the value seen in the Bode plot, which is approximately 10 ohms. After this correction was made, the value for R1 remained close to 10 ohms during all of the fits. Resulting fits with the solution resistance's initial value of 10 ohms for Samples 2, 4, and 7 are shown in Figures 35, 36, and 37.

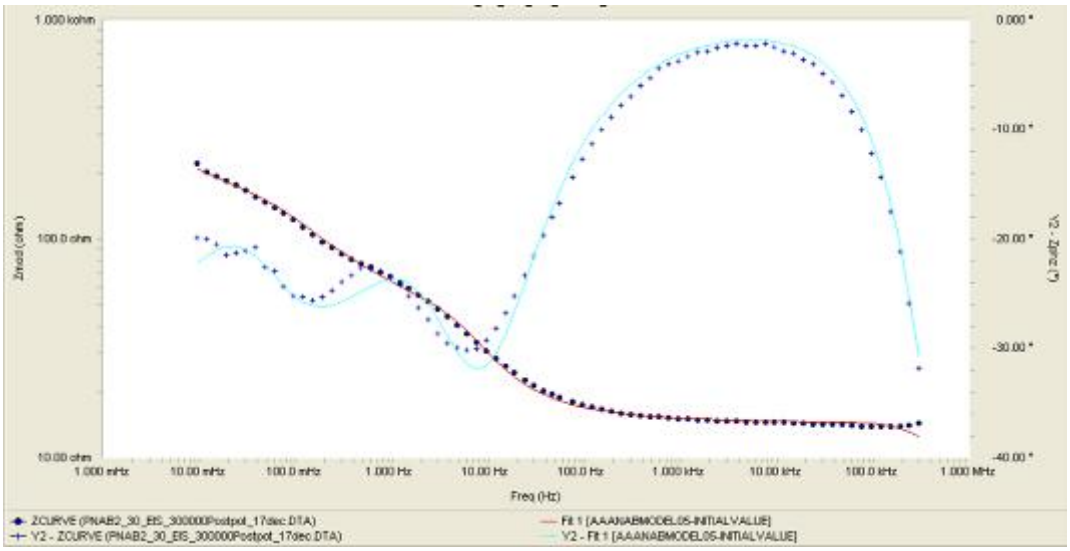

Figure 35. AC (2) NAB SW 30˚C model 5, three RC series. A larger format version of this Figure is at the end of this thesis in the Appendix.

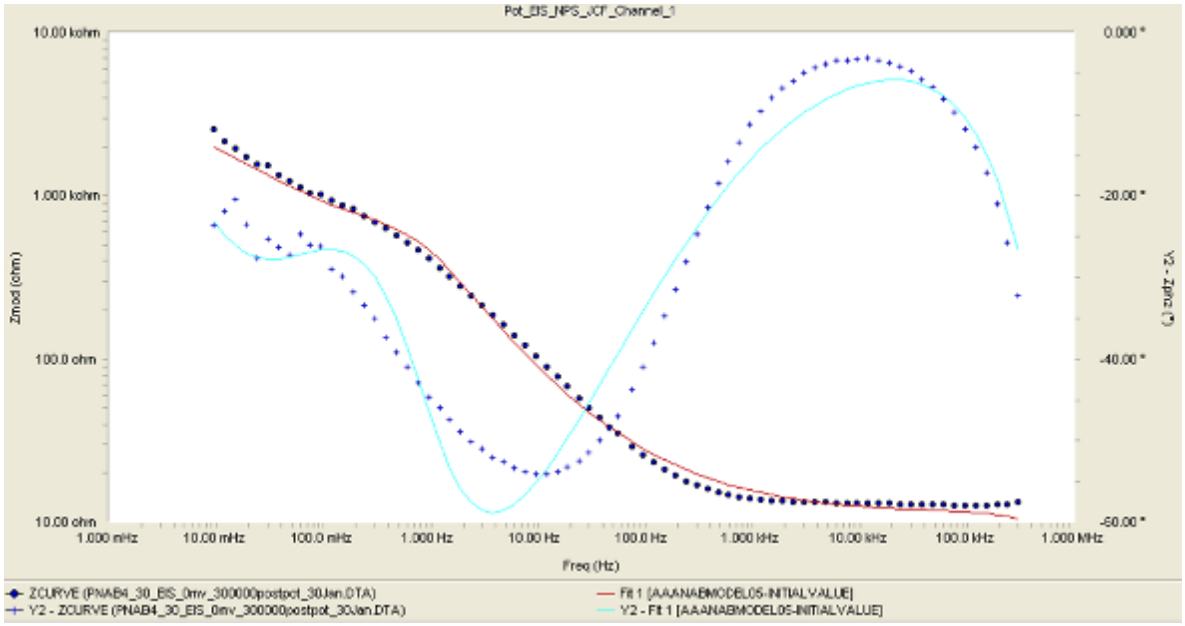

Figure 36. Sample 4 NAB SW 30˚C model 5, three RC series. A larger format version of this Figure is at the end of this thesis in the Appendix.

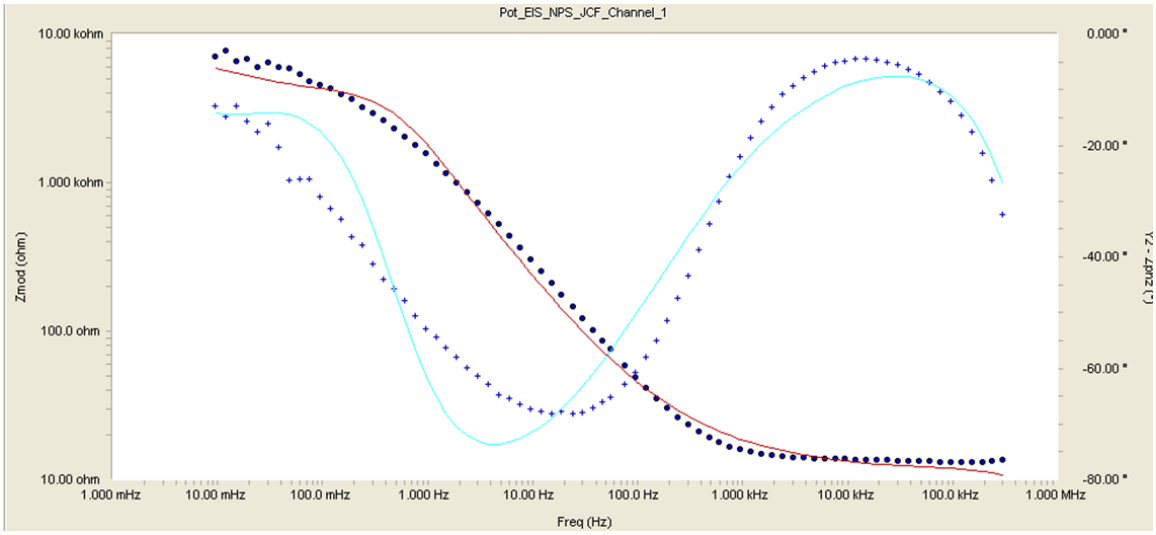

Figure 37. FSP (7) NAB SW 30˚C model 5, three RC series. A larger format version of this Figure is at the end of this thesis in the Appendix.

The values for each circuit element were then placed in an excel spreadsheet for comparison. The values for each circuit element are listed in Table 4.

Table 4. Impedance values model-5 – AC to FSP NAB SW

		Sample Number		
	parameter	2	4	7
Soln Resistance	R1	2.80E-04	2.50E-06	1.03E-03
Double Layer Capt	C2	1.14E-08	4.69E-13	1.50E-14
Warburg Imp	W3	3.99E-02	5.44E+01	4.36E+00
Gerischer Imp	Yo4	1.95E-02	2.39E-03	1.58E-03
Gerischer Imp	K5	3.66E-01	3.67E-02	2.48E-02
RC 1	R6	1.45E+01	1.13E+01	1.14E+01
	C7	1.02E-08	2.30E-08	2.25E-08
RC 2	R8	5.90E-03	438.2	3.66E+03
	C10	1.08E+01	4.41E-04	9.45E-05
RC 3	R10	22.51	3.25E-06	8.14E-09
	C11	1.44E-03	8.04E-06	1.72E-08

The corresponding Excel chart to Table 4 is shown in Figure 38.

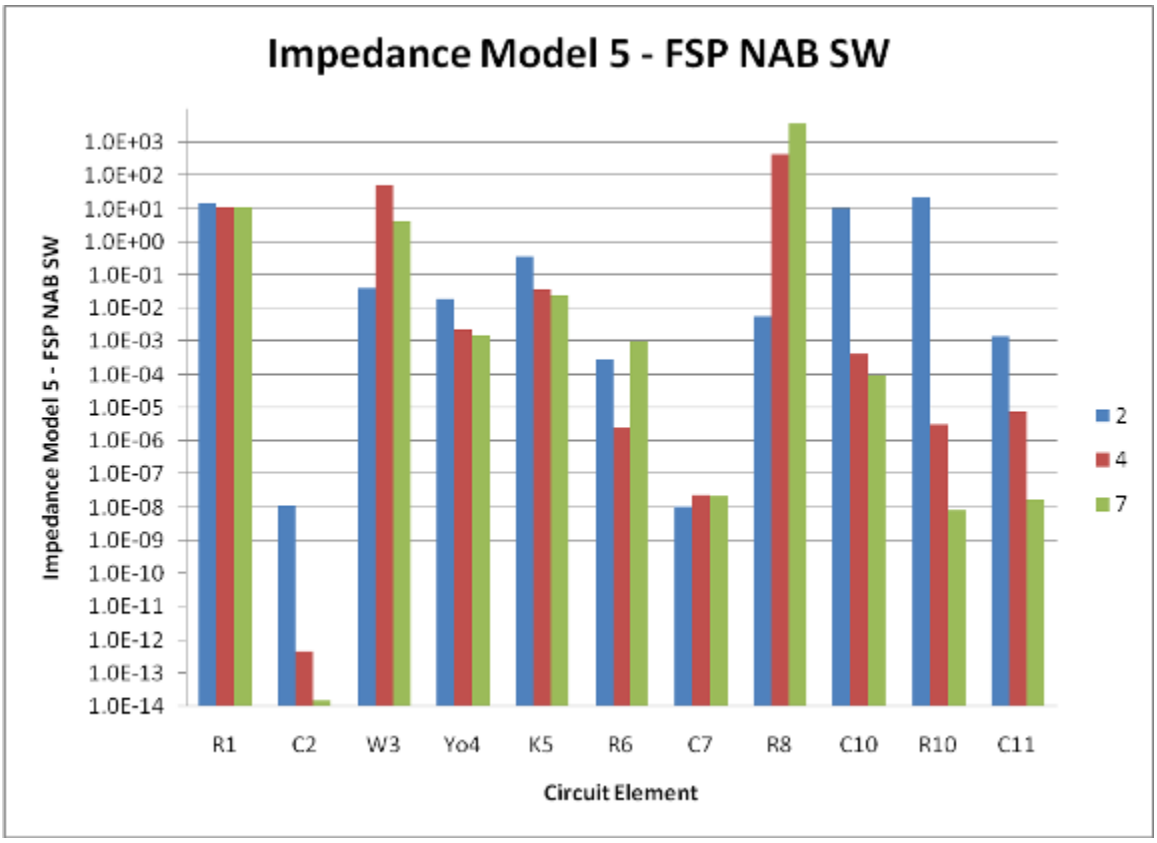

Figure 38. Impedance parameters, model-5, fixed solution resistance

The final model fit to the data was built around the hypothesis that each phase has its own unique porous film (Figure 39).

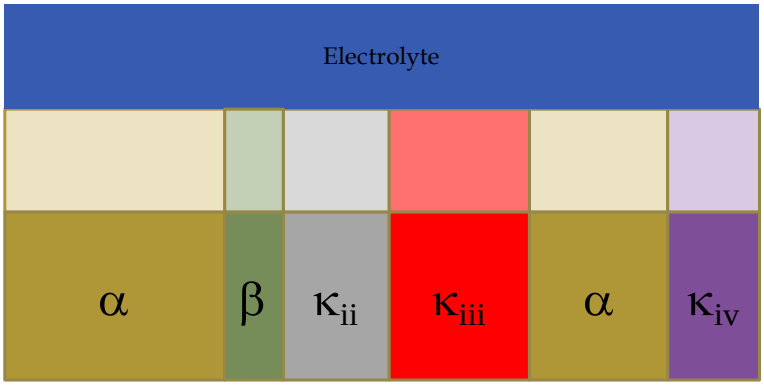

Figure 39. Model-6 physical representation

As a result, the three RC networks were placed in parallel with one another as shown in Figure 40.

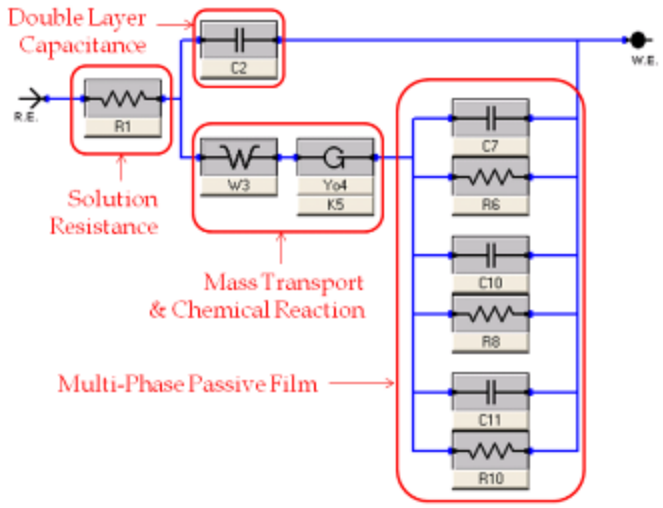

Figure 40. Model-6: three RC parallel network

As in the previous three models, the simplex method was used to fit the EIS data. The initial guess for solution resistance was assumed to be close to 10 ohms. Figures 41, 42 and 43 show the fit of model-6 on data from Samples 2, 4, and 7 respectively.

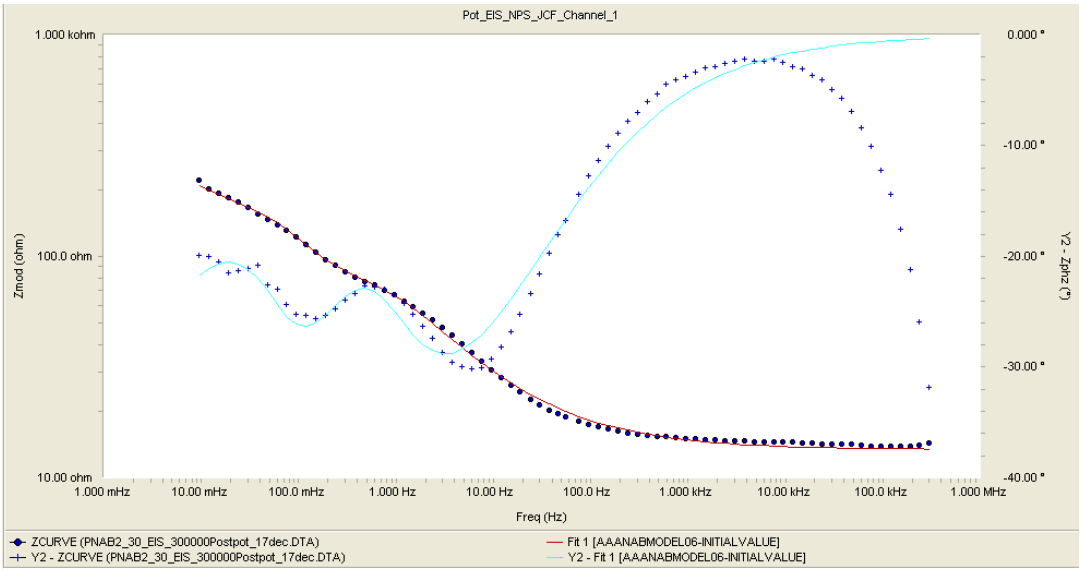

Figure 41. AC (2) NAB SW 30˚C model-6, three RC parallel. A larger format version of this Figure is at the end of this thesis in the Appendix.

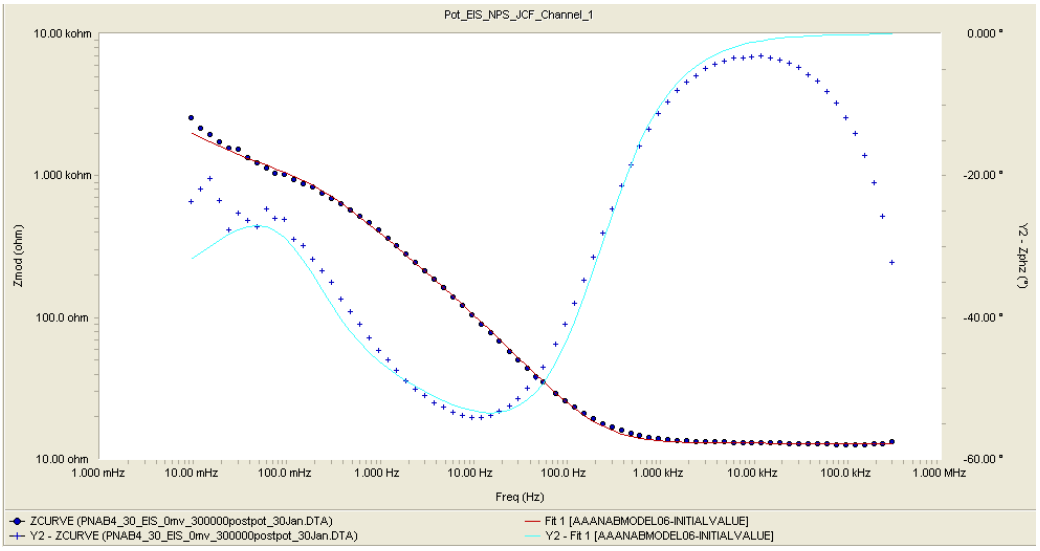

Figure 42. FSP (4) NAB SW 30˚C model-6, three RC parallel. A larger format version of this Figure is at the end of this thesis in the Appendix.

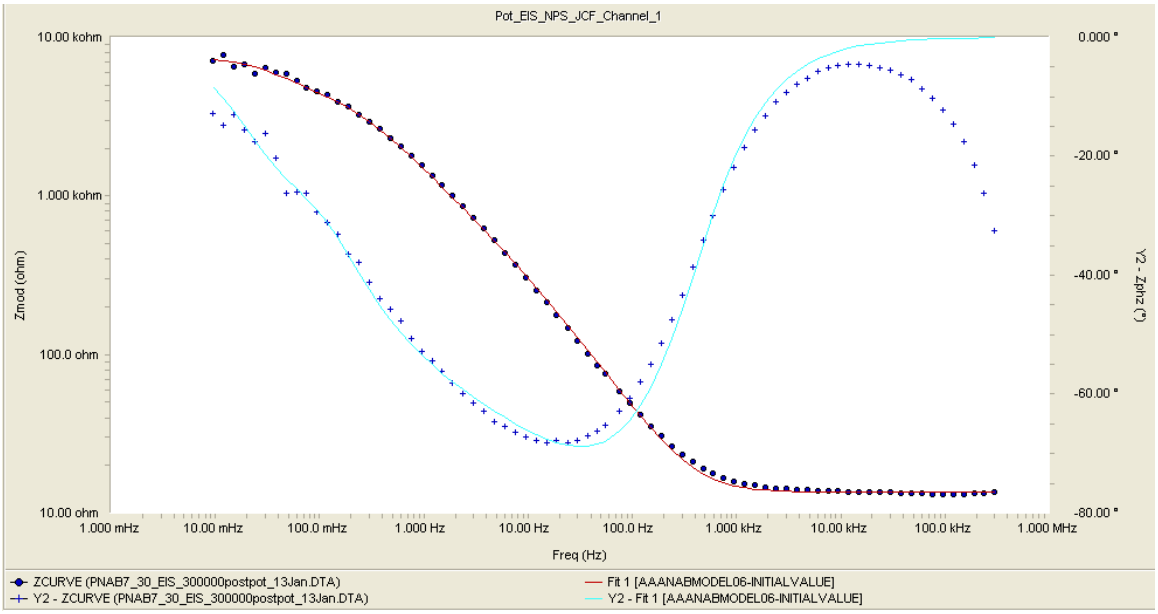

Figure 43. FSP (7) NAB SW 30˚C model-6, three RC parallel. A larger format version of this Figure is at the end of this thesis in the Appendix.

As shown in these figures, the phase fit is good, but most importantly, the fit of model-6 to the amplitude data is extremely good over the entire frequency range. The parameter values obtained in modeling arecomplied in excel and shown in Table 5.

Table 5. Impedance values model-6 – AC to FSP NAB SW

		Sample Number		
	Parameter	2	4	7
Soln Resistance	R1	13.42	13.01	13.58
Double Layer Capt	C2	6.43E-11	5.85E-05	3.00E-05
Warburg Imp	W3	4.15E-02	2.78E-03	18.07
Gerischer Imp	Yo4	7.98E-03	1.41E-03	2.23E-04
Gerischer Imp	K5	6.076	1.10E+00	1.09E+00
RC 1	R6	62.28	5.61E-04	1.67E+05
	C7	7.25E-05	1.96E-04	7.82E-07
RC 2	R8	2.44E+03	4.38E-05	5.72E+07
	C10	3.41E-02	4.03E-03	1.56E-03
RC 3	R10	7.30E+03	9.50E-06	3.18E+03
	C11	1.38E-06	2.38E-07	5.16E-08

Next, the values were placed in chart, Figure 44, to facilitate viewing the changes in parameters from the AC to the FSP conditions.

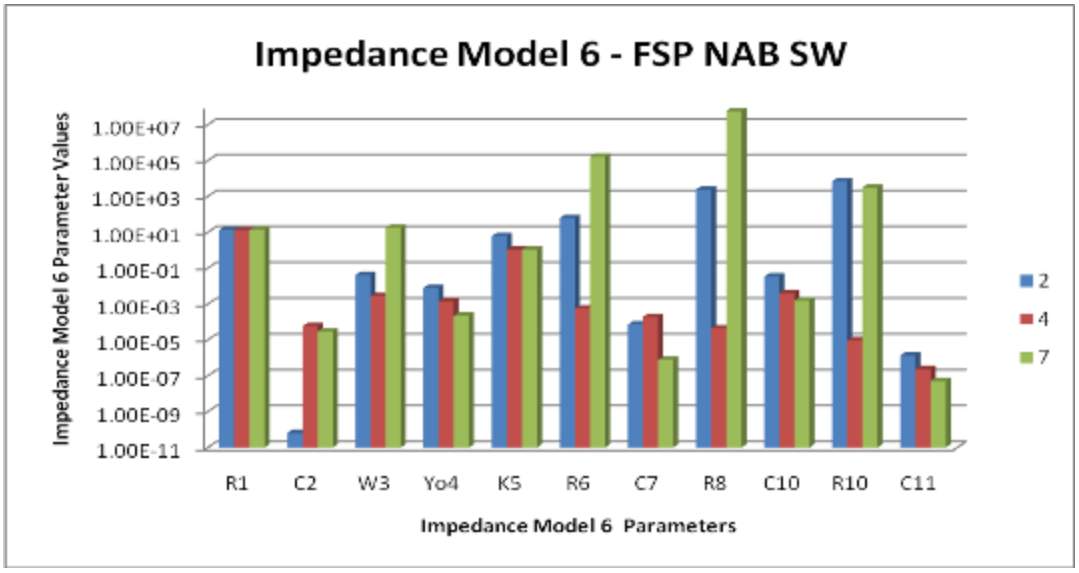

Figure 44. Impedance parameters, model-6, fixed solution resistance

Table 5 and Figure 44 show unambiguously that FSP changes the value for Warburg impedance, R6, and R8, by three orders of magnitude. As the amount of FSP increases, these values increase. The change in these parameters validates the increase shown in Figure 19 where the polarization resistance increased from Samples 2 to 7. Thus, it can be concluded, that FSP increases the resistance of NAB to corrosion by increasing the polarization resistance and the resistance of mass transferring through the film (improved diffusion performance).

E. MICROSCOPY

Pre and post EIS testing, the samples were observed in the scanning electron microscope. Figure 45 shows the stir zone and as cast region as well as the distinct boundary between them.

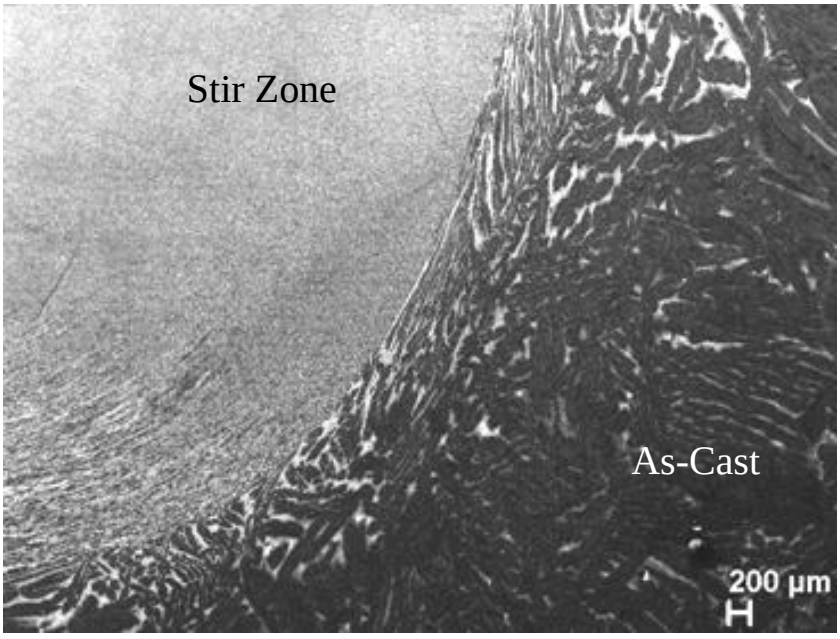

Figure 45. FSP zones and boundary, from [17]

Each of these regions was then imaged at a higher magnification. The cast and FSP regions can each be seen in Figure 46. The bottom right image shows the eutectoid region, or AC region, consisting of α and κ_{iii} (Fe_3Al). In the predominately α region there

are fine κ_{ii} cryastallites. The κ_{iii} phase (NiAl) of the AC section also contains the fine κ_{ii} precipitates crystallites. The κ_{ii} particles in the NiAl phase may serve as pit initiation sites. The FSP material shows a much more homogenized mixture of α and κ phases. This refinement of NAB is linked to the improved resistance to corrosion.

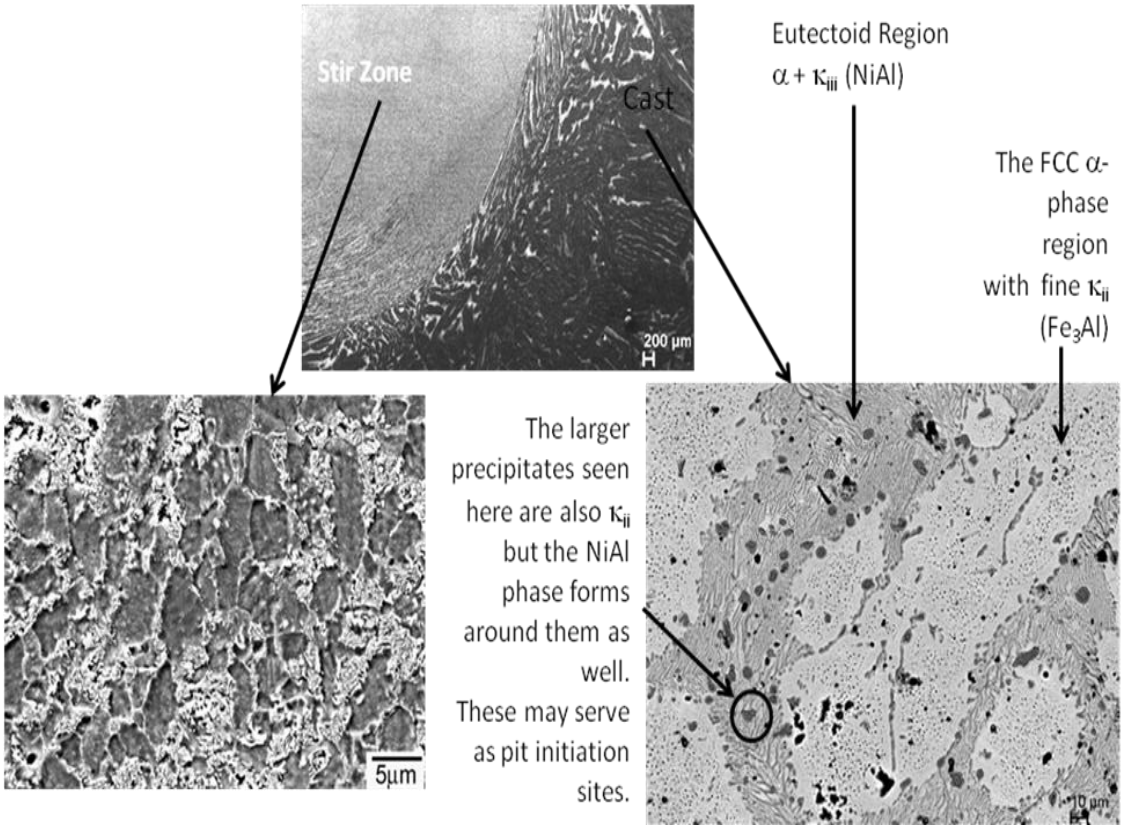

Figure 46. Pre film formation FSP NAB, from [17]

A more indepth study of the effects of FSP on microstructure is discussed by Nelson [8].

After corrosion testing, Samples 2 and 7 were again imaged using the SEM. Sample 2 is shown in Figure 47. The morphology of the passive film shows two distinct regions: one oxide that covers the FCC α region and another that covers the lamellar α and κ_{iii} region. The former oxide shows a uniform dispersion of round oxide particles, while the later shows an oxide film with facetted growth. These regions of facetted growth form at pit locations on the NAB's passive film.

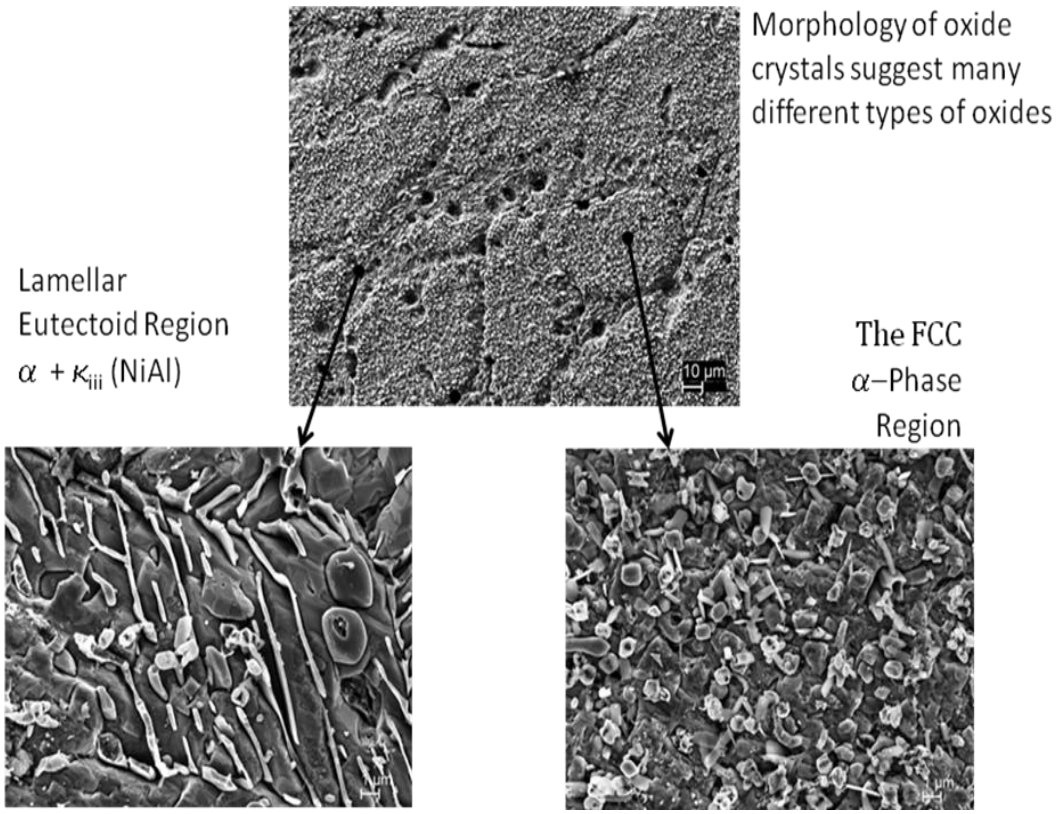

Figure 47. AC NAB (2) post-corrosion testing, from [17]

A closer examination of the AC passive film is shown in Figure 48. These micrographs show more clearly the facetted growth and multiple surface oxide regions, including pits. The existence of different oxides present at the surface supports the original hypothesis that each underlying NAB phase has its own unique passive film.

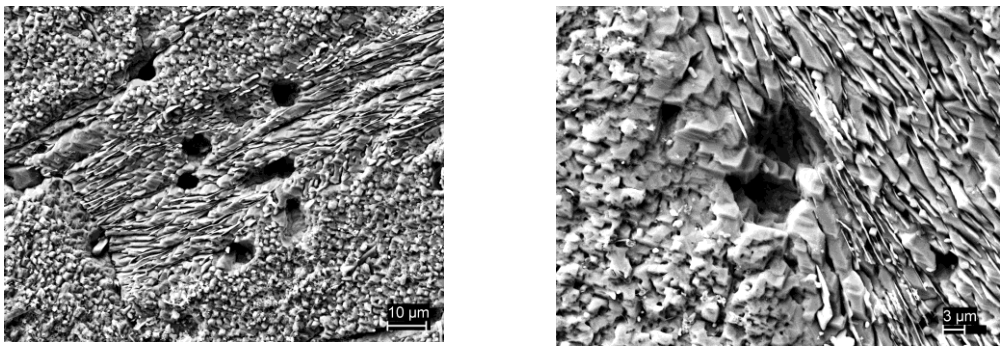

Figure 48. AC NAB (2) post corrosion testing pitting, from [17]

After viewing the AC NAB film, the FSP sample's film was also imaged. The film on the surface of Sample 7 was a uniform oxide layer with no pitting as shown in Figure 49.

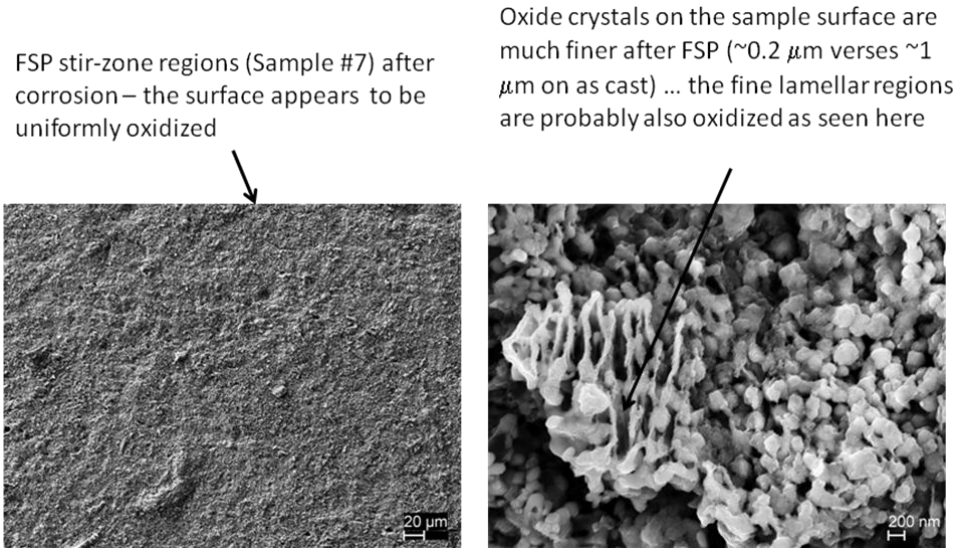

Figure 49. FSP NAB (7) post corrosion testing, from [17]

A closer inspection of this film revealed finer oxide crystals than those that were present in the AC passive film. Most notably, the refined film still showed regions of lamellar oxide growth attributed to the lamellar eutectoid region of the FSP surface, which itself is much finer than the original AC material. Again, no pitting was observed

in the FSP film. The increase in corrosion resistance of the FSP NAB seen in CP and EIS testing was validated by the integrity of the passive film imaged on the surface of Sample 7.

F. FUTURE WORK

In addition to the work already done, a more in depth study of the physical film formed on the surface of NAB should be conducted. Using focused ion beam (FIB) and SEM, the transverse view of the passive film and underlying phase could be imaged. This image would solidify the results of this paper. Another way to connect the microstructural changes created in FSP with corrosion resistance would be to measure the volume fraction of each phase present on the surface of each sample and fit the EIS values from modeling to each specific phase.

V. CONCLUSION

By using a wide range of techniques, the corrosion resistance of friction stir processed, nickel aluminum bronze (FSP NAB) was evaluated. Cyclic polarization (CP) testing revealed the stability of FSP passive films over a wider range of potentials and a reduction in the cathodic current, which showed a decrease in the reduction reactions that drive corrosion.

Electrochemical impedance spectroscopy (EIS) data also showed an increase in the passivation resistance at low frequencies. This data was modeled using a wide range of electric circuit models to represent corrosion microstructures of varying complexity. The simplest model that still fit the data was model number-6, a three RC parallel model. This model fit the hypothesis that each phase of NAB forms a unique oxide on its surface when placed in a corrosive environment.

SEM images were used to verify the integrity and to determine the microstructural morphology of the FSP passive film. Images pre- and post corrosion testing revealed a more uniform surface and passive film formed on the FSP Sample (7) compared with as-cast material.

In order to be considered for use in processing and repair, FSP needed to demonstrate an increase in material performance, which was shown in previous experiments, and maintain or improve upon the alloy's original corrosion resistance. This study showed FSP increased the corrosion resistance of NAB; thus, further consideration for it as a surface treatment on propellers may be taken.

THIS PAGE INTENTIONALLY LEFT BLANK

LIST OF REFERENCES

[1] M. Sahoo, "Structure and mechanical properties of slow-cooled nickel aluminum bronze alloy C95800," *AFS Trans,* vol. 90, pp. 913–926, 1982.

[2] R. Pidaparti, B. Aghazadeh, A. Whitfield, A. Rao, and G. Mercer, (2010). Classification of corrosion defects in NiAl bronze through image analysis. *Corrosion Science,* vol. 52, no. 11, pp. 3661–3666.

[3] W. Thomas, E. Nicholas, J. Needham, M. Murch, P. Temple-Smith, and C. Dawes, *Friction-stir butt welding*, GB Patent No. 9125978.8, International patent application No. PCT/GB92/02203, 1991.

[4] F. Hasan, A. Jahanafrooz, G. W. Lorimer, N. Ridley. "The Morphology, crystallography, and chemistry of phases in as-cast nickel-aluminum bronze," *Metallurgical and Materials Transactions A*, vol. 13, no. 8, p. 1337, 1982 [doi:10.1007/BF02642870].

[5] Callcut, V. (2002, August). *Aluminum bronzes- part II*. Retrieved from http://www.copper.org/publications/newsletters/innovations/2002/08/aluminum2.html

[6] "ASTM Standard B148 - 97(2009) Standard Specification for Aluminum Bronze Sand Castings," ASTM International, West Conshohocken, PA. DOI:10.1520/B0148-97R09. Retrieved from www.astm.org.

[7] M. Pourbaix. *Atlas of Electrochemical Equilibria in Aqueous Solutions*. Oxford, New York: Pergamon Press, 1974.

[8] E. A. Nelson, "Microstructural Effects of Multiple Passes during Friction Stir Processing of Nickel Aluminum Bronze," M.S. thesis, Dept. Mech. Eng., Naval Postgraduate School, Monterey, CA, December 2009.

[9] M. D. Fuller, "Friction Stir Processing and Fusion Welding in Nickel Aluminum Propeller Bronze," M.S. Thesis, Dept. Mech. Eng., Naval Postgraduate School, Monterey, CA, 2006.

[10] K. Tretheway and R. Chamberlain, *Corrosion for Science and Engineering* Second Edition. Longman Scientific & Technical, 1995, p. 196.

[11] T. McNelley and K. Oh-Ishi, "Microstructural modification of as-cast NiAl bronze by friction stir processing," *Metallurgical and Materials Transactions A*, vol. 35A, pp. 2004–2951. September 2004.

[12] T. R. McNelley and K. Oh-Ishi, "The influence of friction stir processing parameters on microstructure of as-cast NiAl bronze." *Metallurgical and Materials Transactions A,* vol. 36A, pp. 1575–1585. June 2005.

[13] D. Lenard, C. Bayley, and B. Noren. "Detection of selective phase corrosion of Nickel Aluminum Bronze in sea water by electrochemical frequency modulation." Presented at Proceedings of the 2009 DOD Corrosion Conference, Washington, D.C., August, 2009.

[14] J. Farmer, "High-Performance Corrosion-Resistant Materials: Fe-Based Amorphous-Metal Coatings & Composite Surfaces," *Encyclopedia of Composite Materials*, vol 2, 2nd ed. John Wiley and Sons, New York, NY, 2008.

[15] A. J. Bard, L. R. Faulkner, *Electrochemical Methods, Fundamentals and Applications*. John Wiley & Sons, New York, 1980.

[16] Gamry instruments. "Basics of electrochemical impedance spectroscopy." Application note, 2009. Retrieved April 1, 2011, from http://www.gamry.com/App_Notes/EIS_Primer/Basics_Of_%20EIS.pdf.

[17] J. C. Farmer, S. Menon, P. S. LeGrand, and L. H. Hackel. "As-cast friction stir processed Ni-Al Bronze: electrochemical studies of passive film formation and corrosion in Monterey Bay seawater at 30 degrees. Presented at Proceedings of the 219th meeting of the Electrochemical Society, Montreal, Canada, May 2011.

APPENDIX

The electrochemical impedance spectroscopy figures from the text are reproduced below in the order of their appearance in the original text in larger format for ease of viewing.

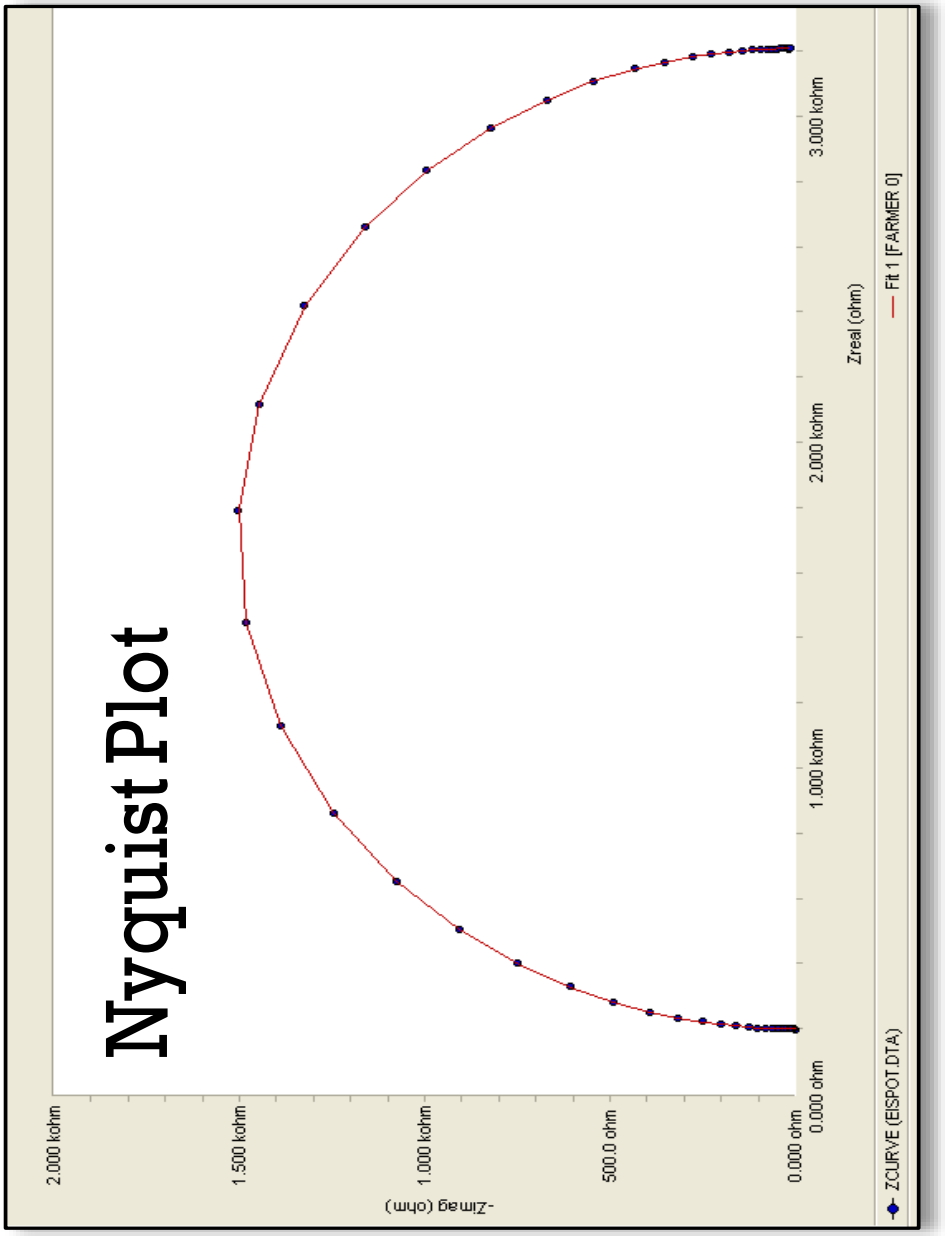

Figure 8: The Nyquist plot for the equivalent circuit shown in Figure 12

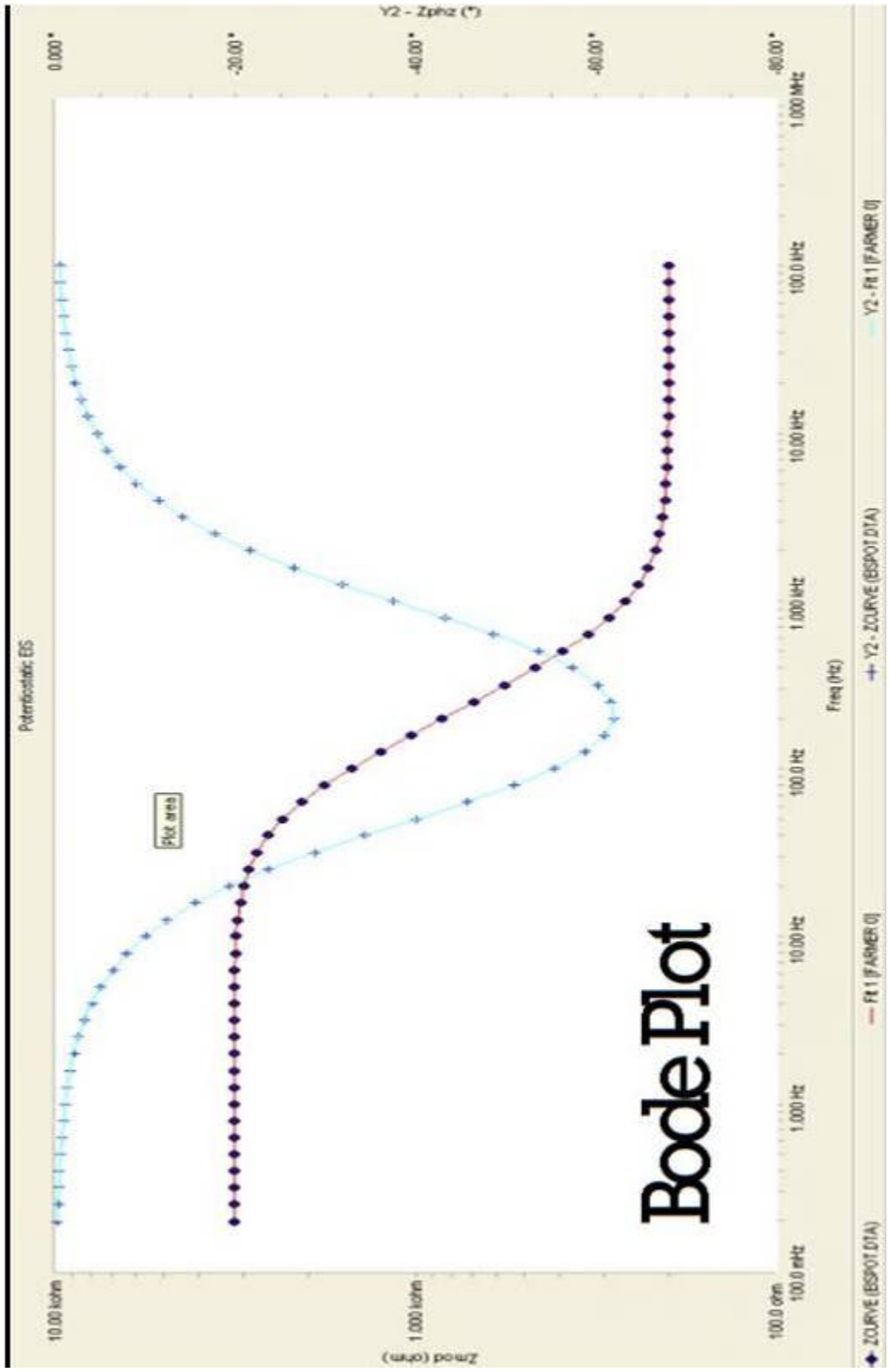

Figure 9: Bode plot for the equivalent circuit shown in Figure 12

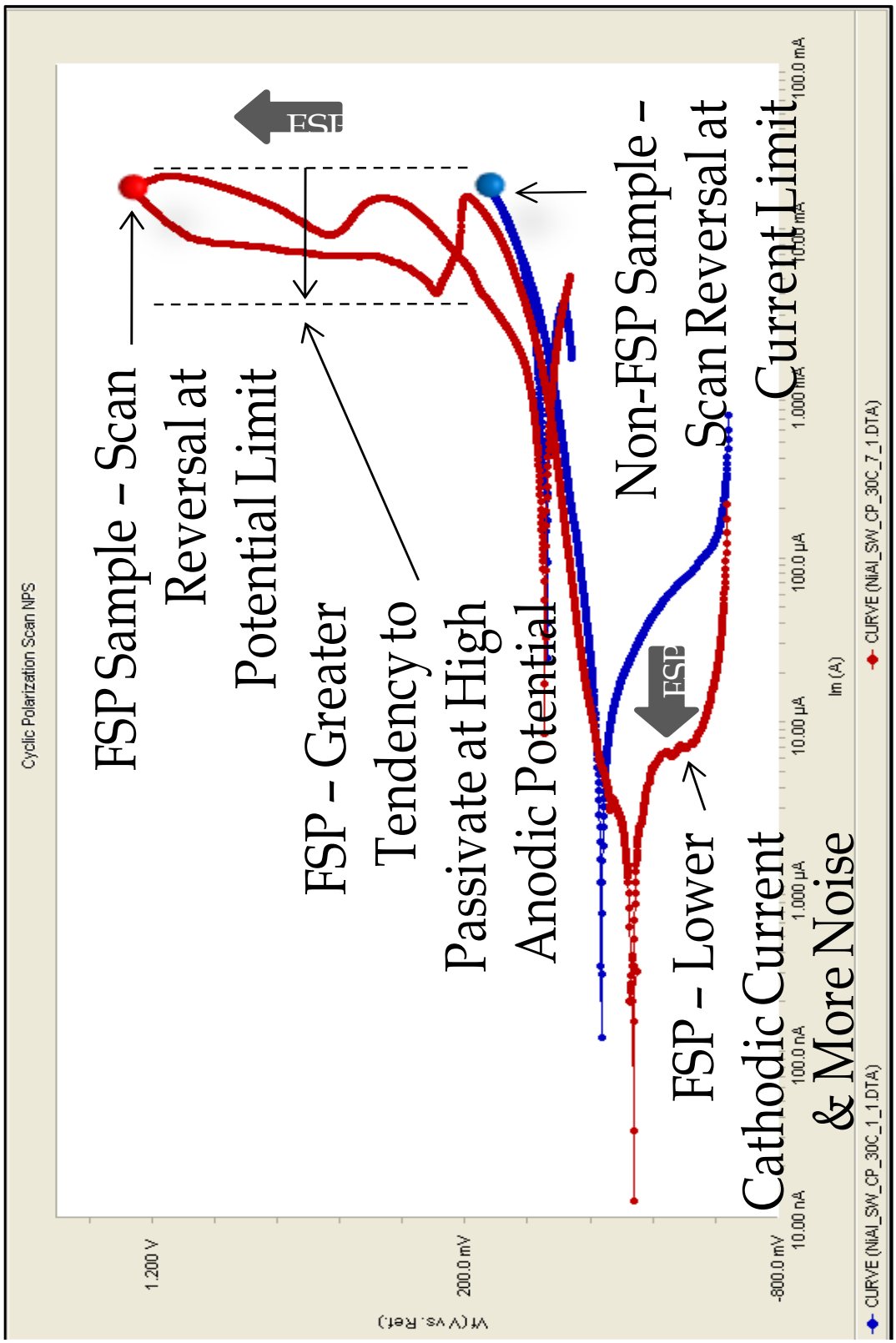

Figure 16: Cyclic polarization overlay of Samples 2 and 7 from [17]

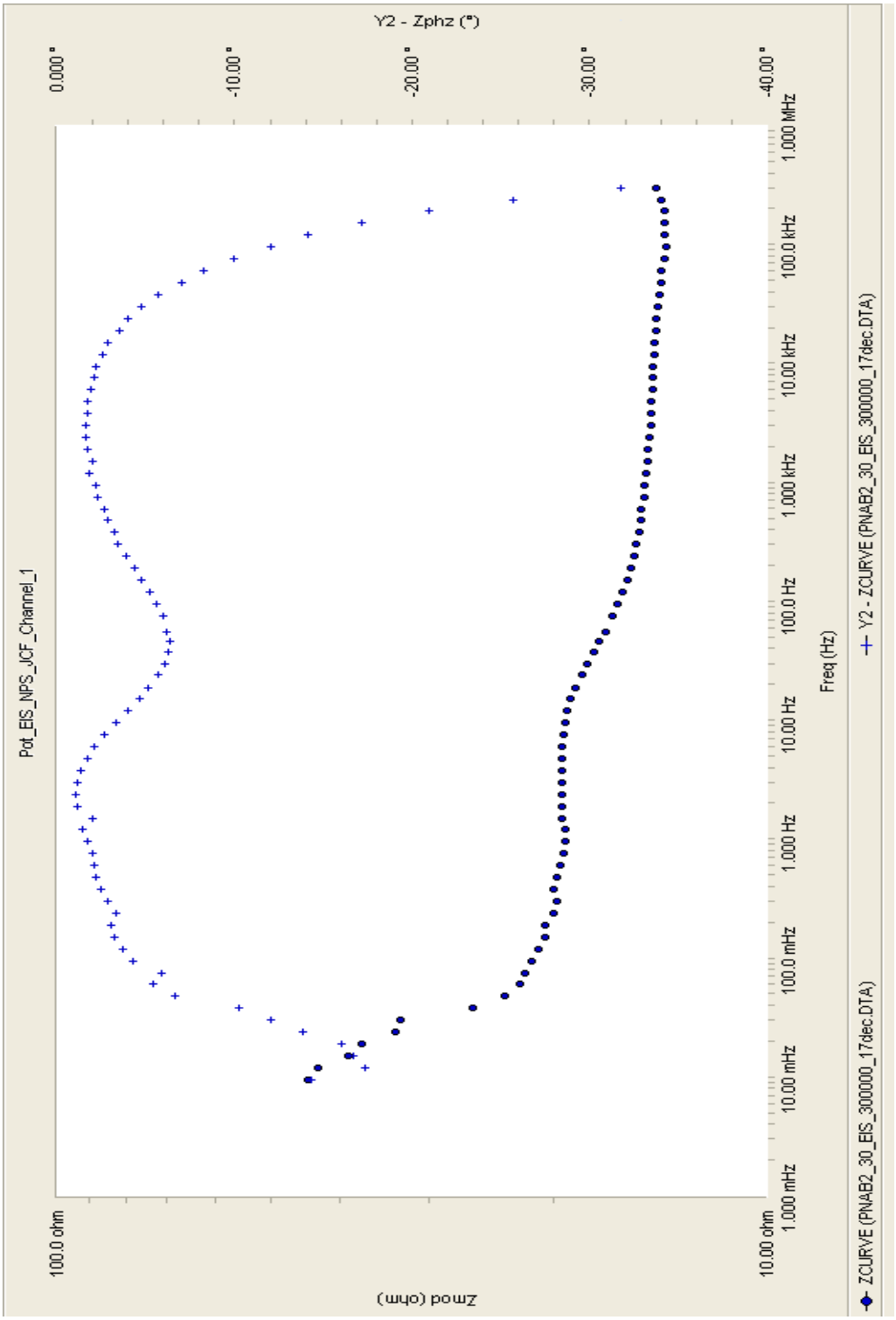

Figure 17: Bode plot for Sample 2 (AC NAB), 30˚C SW

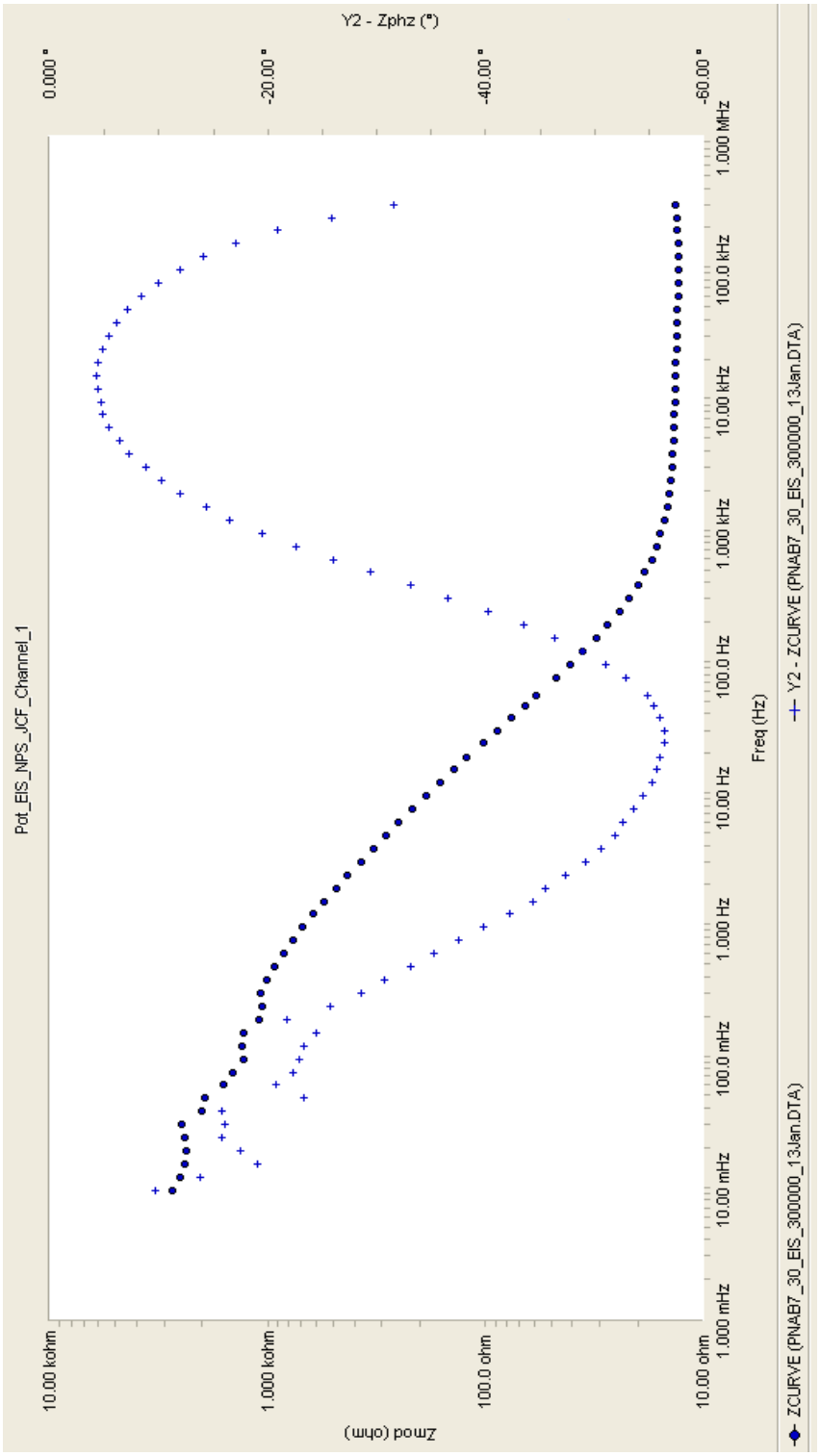

Figure 18: Bode plot for Sample 7 (FSP NAB), 30˚C SW

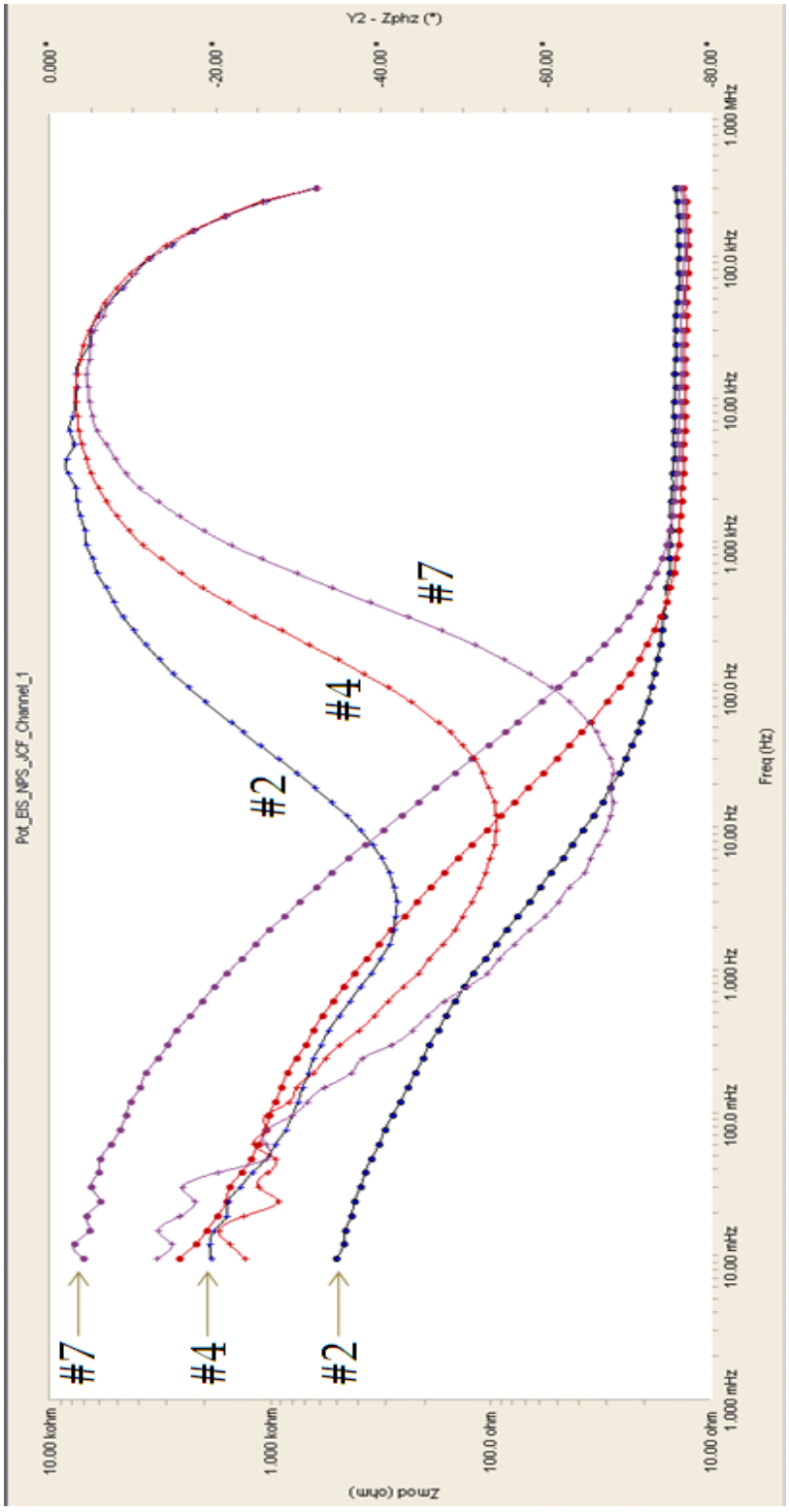

Figure 19: Overlay Bode plot, Samples 2, 4 and 7, 30˚C SW

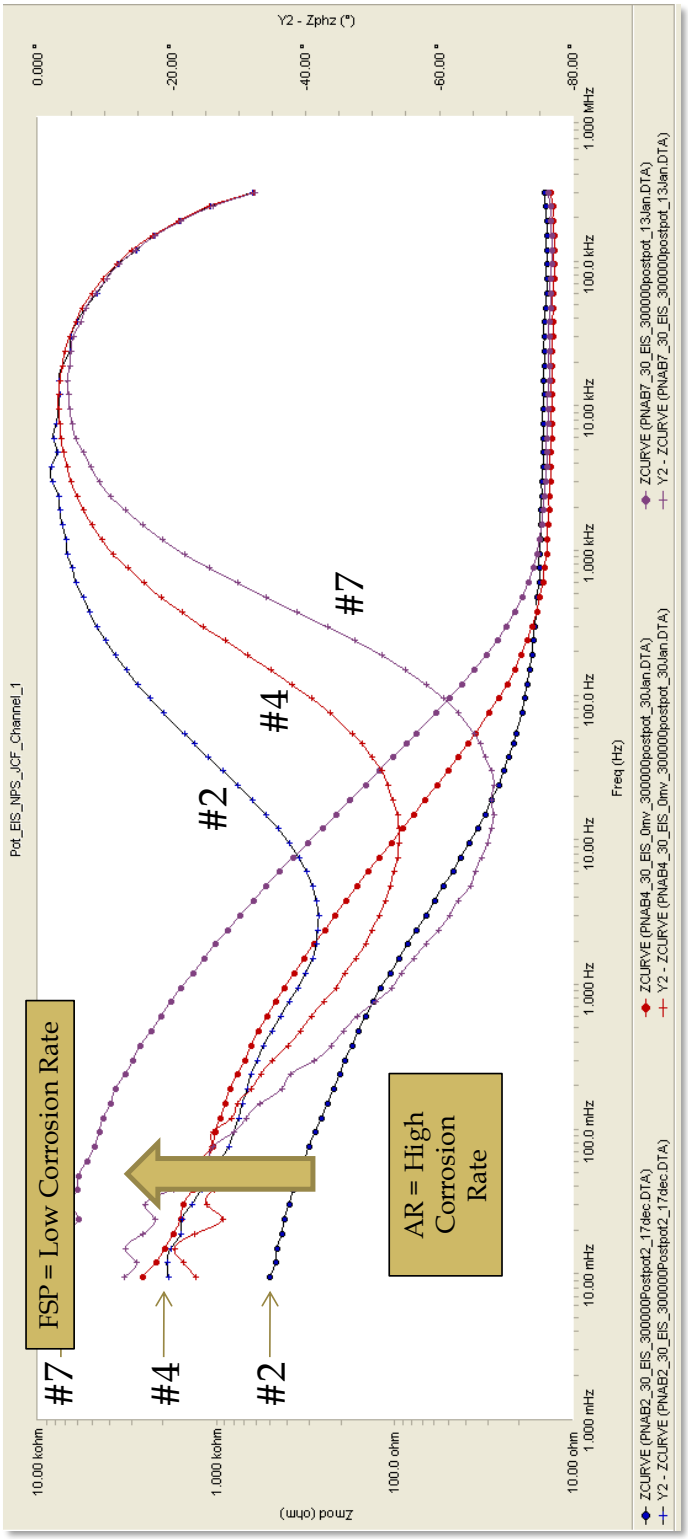

Figure 20: Annotated overlay Bode plot, Samples 2, 4 and 7, 30˚C SW

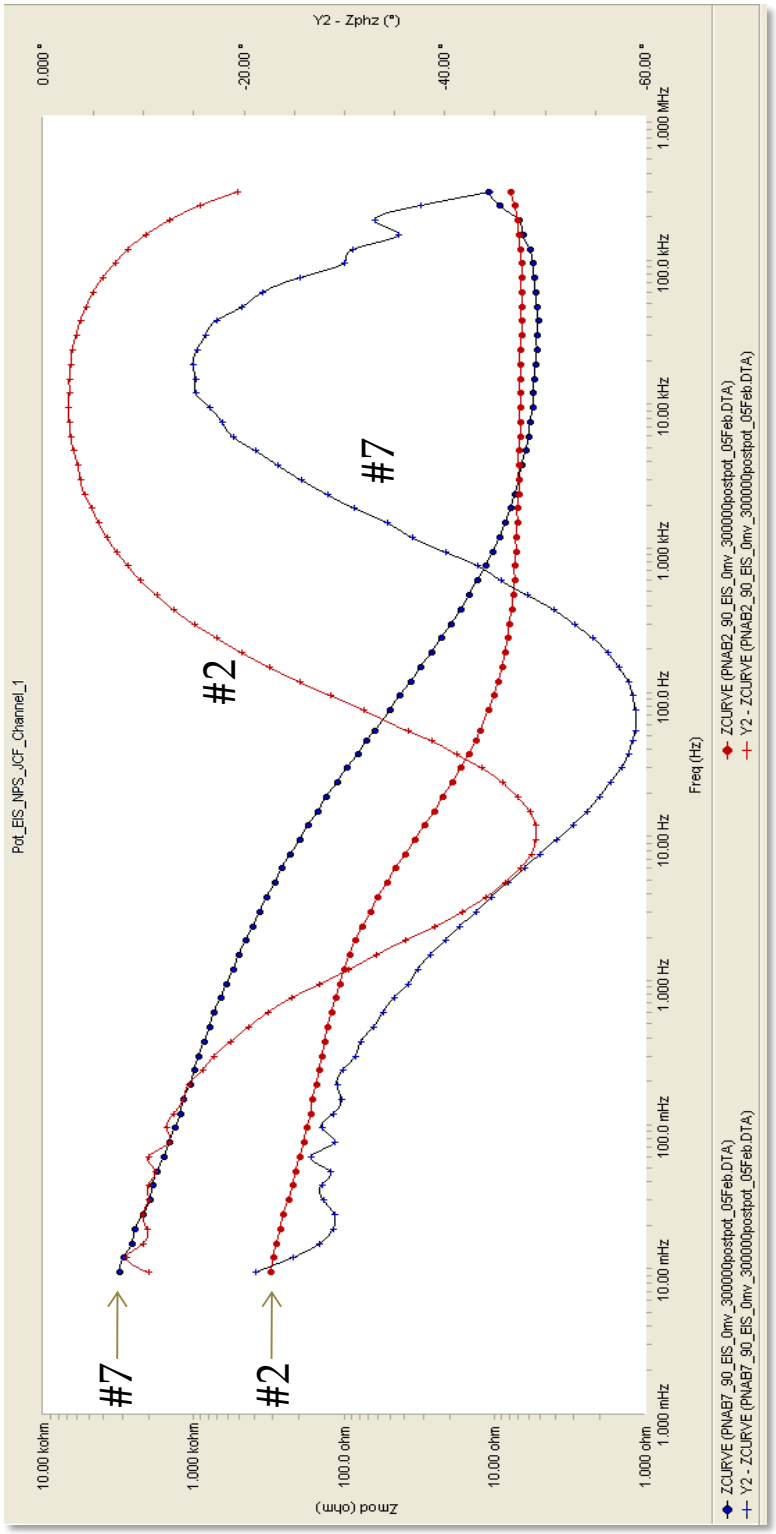

Figure 21: Overlay Bode plot, Samples 2 and 7, 90˚C

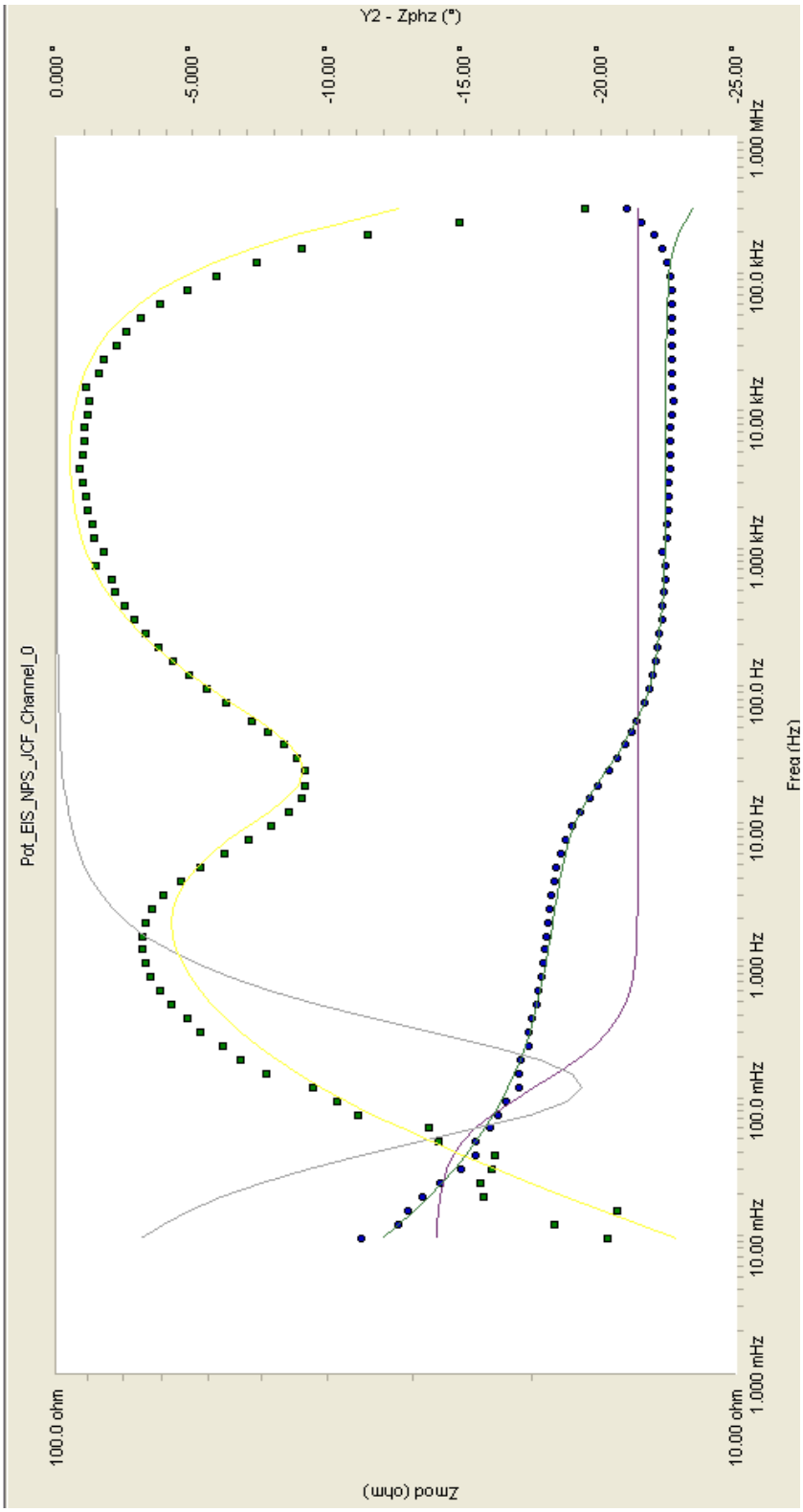

Figure 27: FSP NAB EIS models-0 and 15

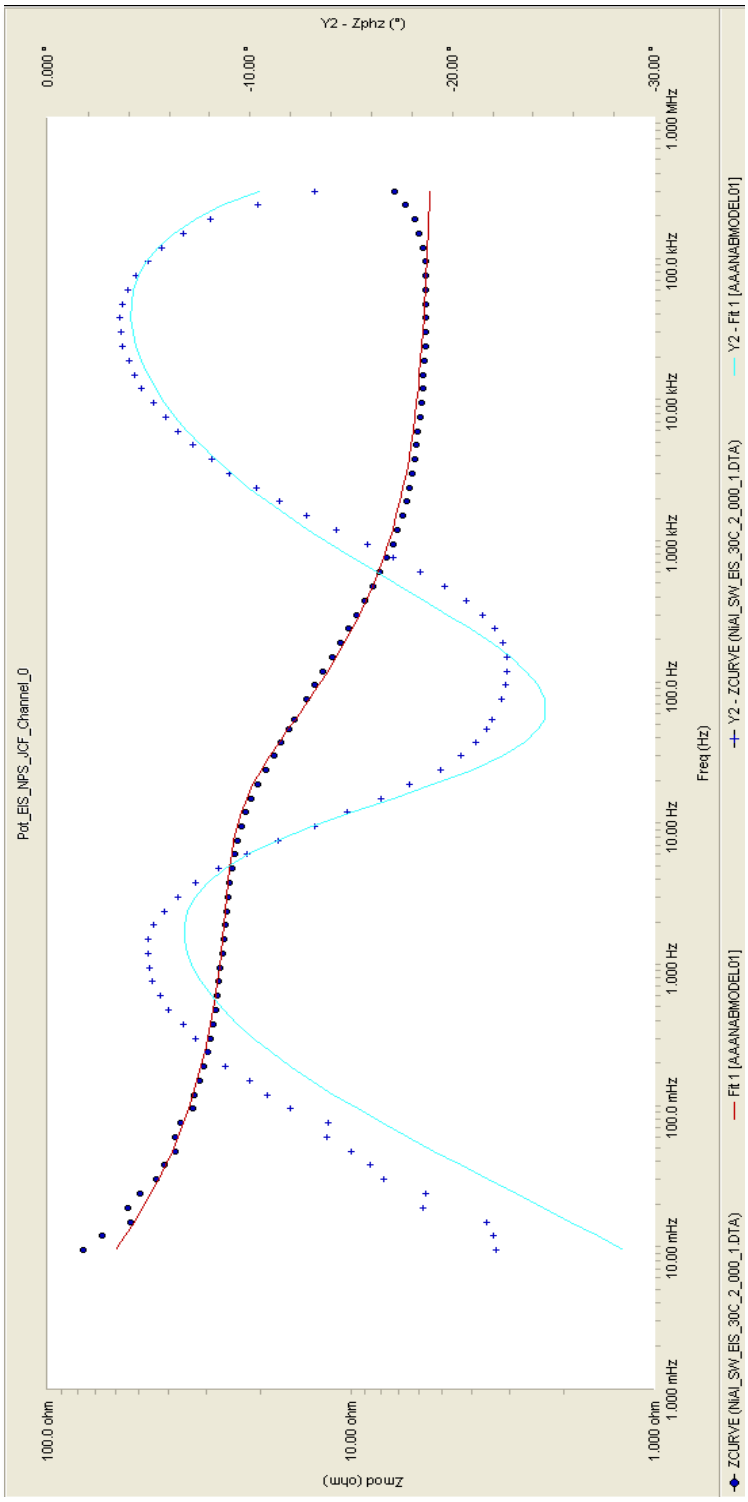

Figure 29: AC (2) NAB SW 30°C model-1 unified transmission line

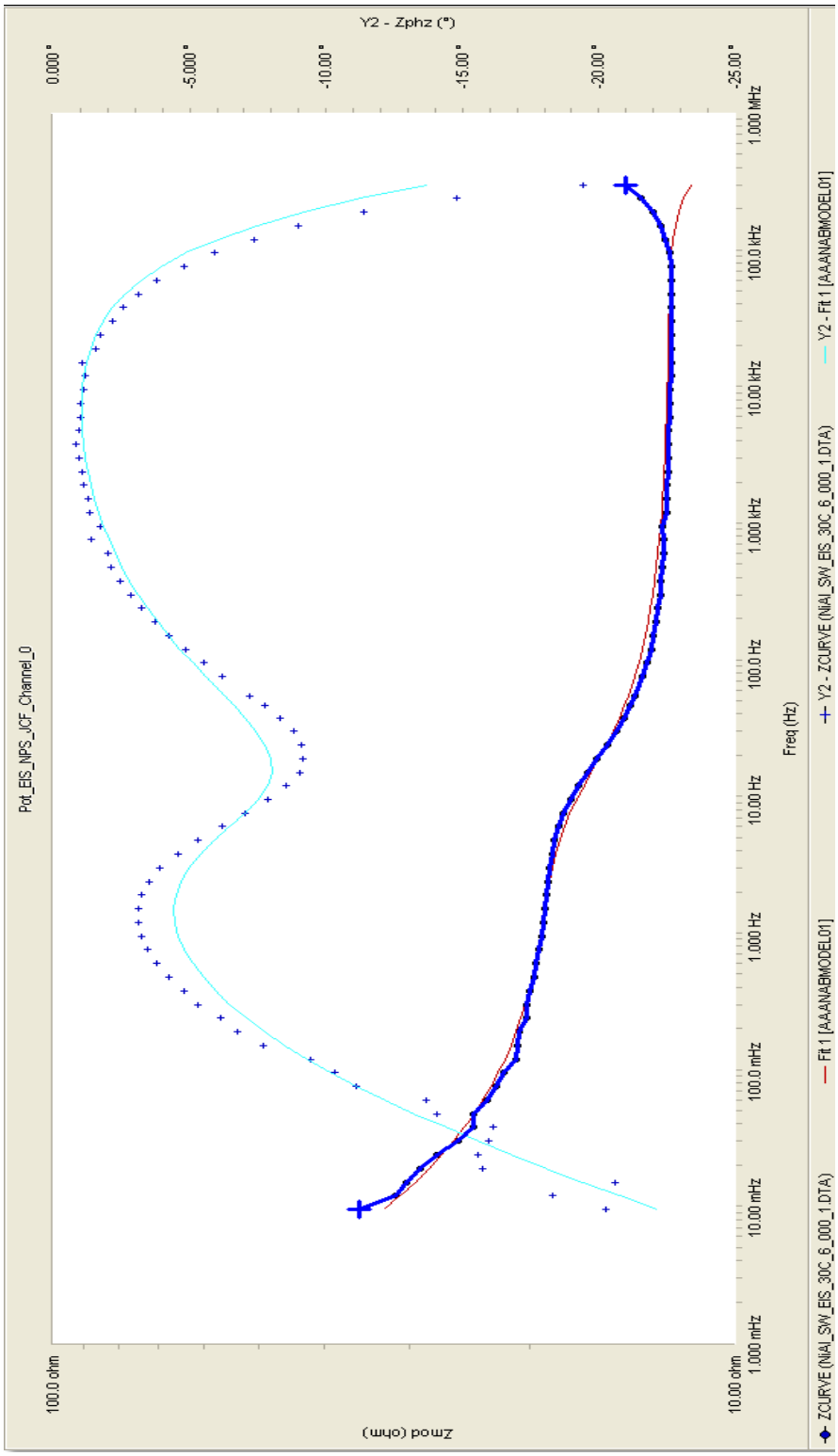

Figure 30: FSP (6) NAB SW 30°C model-1 unified transmission line

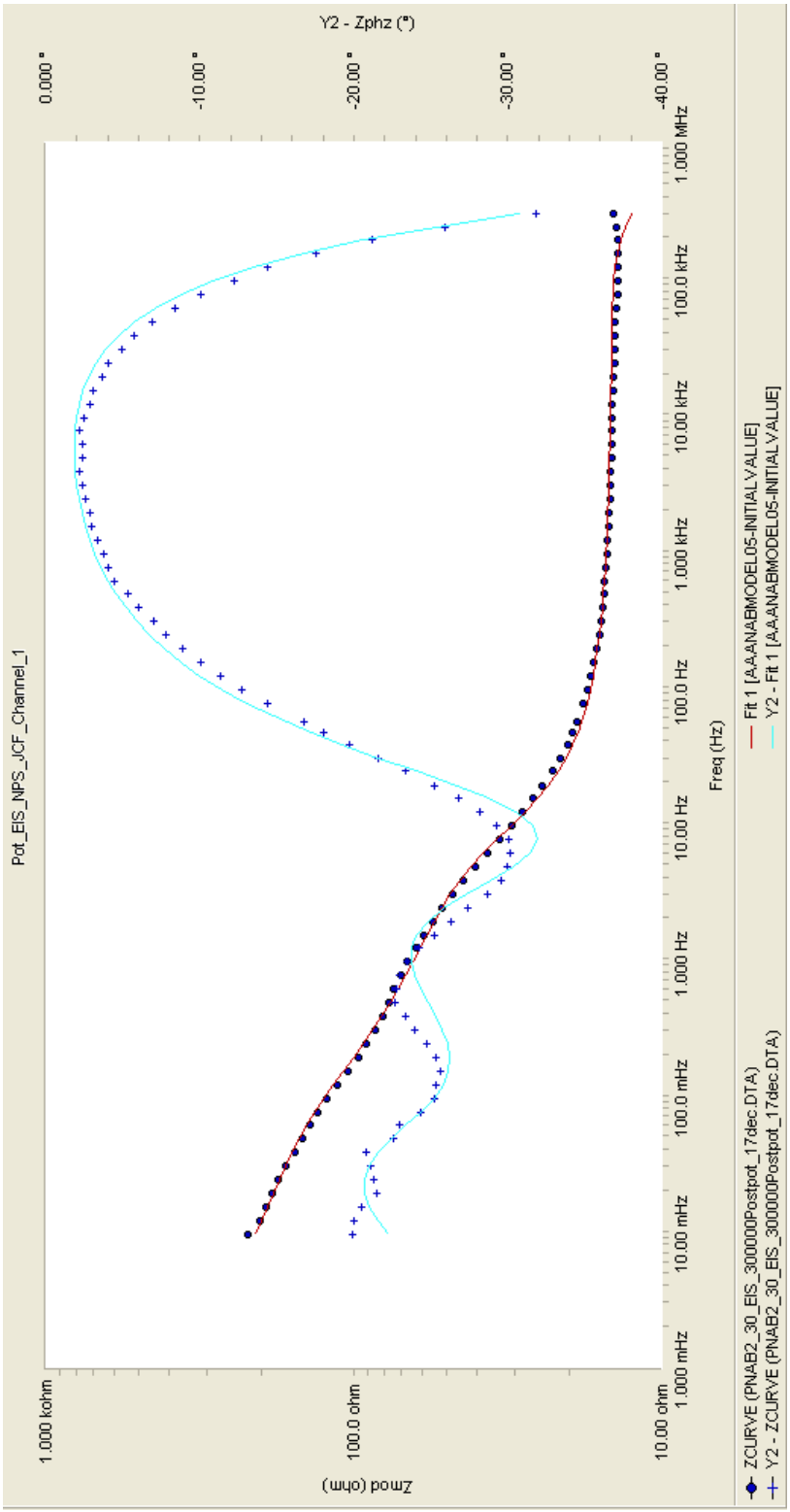

Figure 35: AC (2) NAB SW 30˚C model 5, three RC series

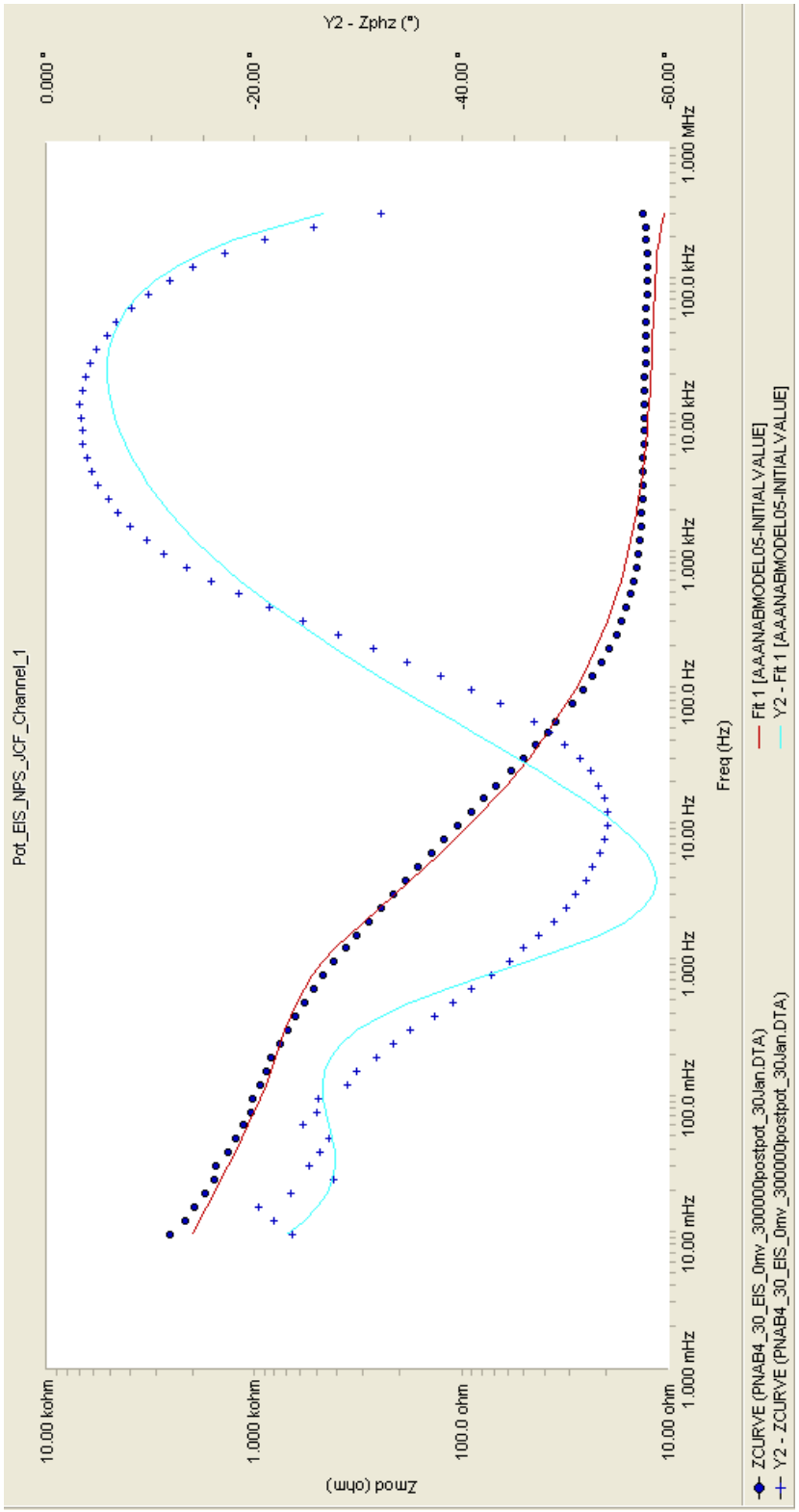

Figure 36: Sample 4 NAB SW 30˚C model 5, three RC series

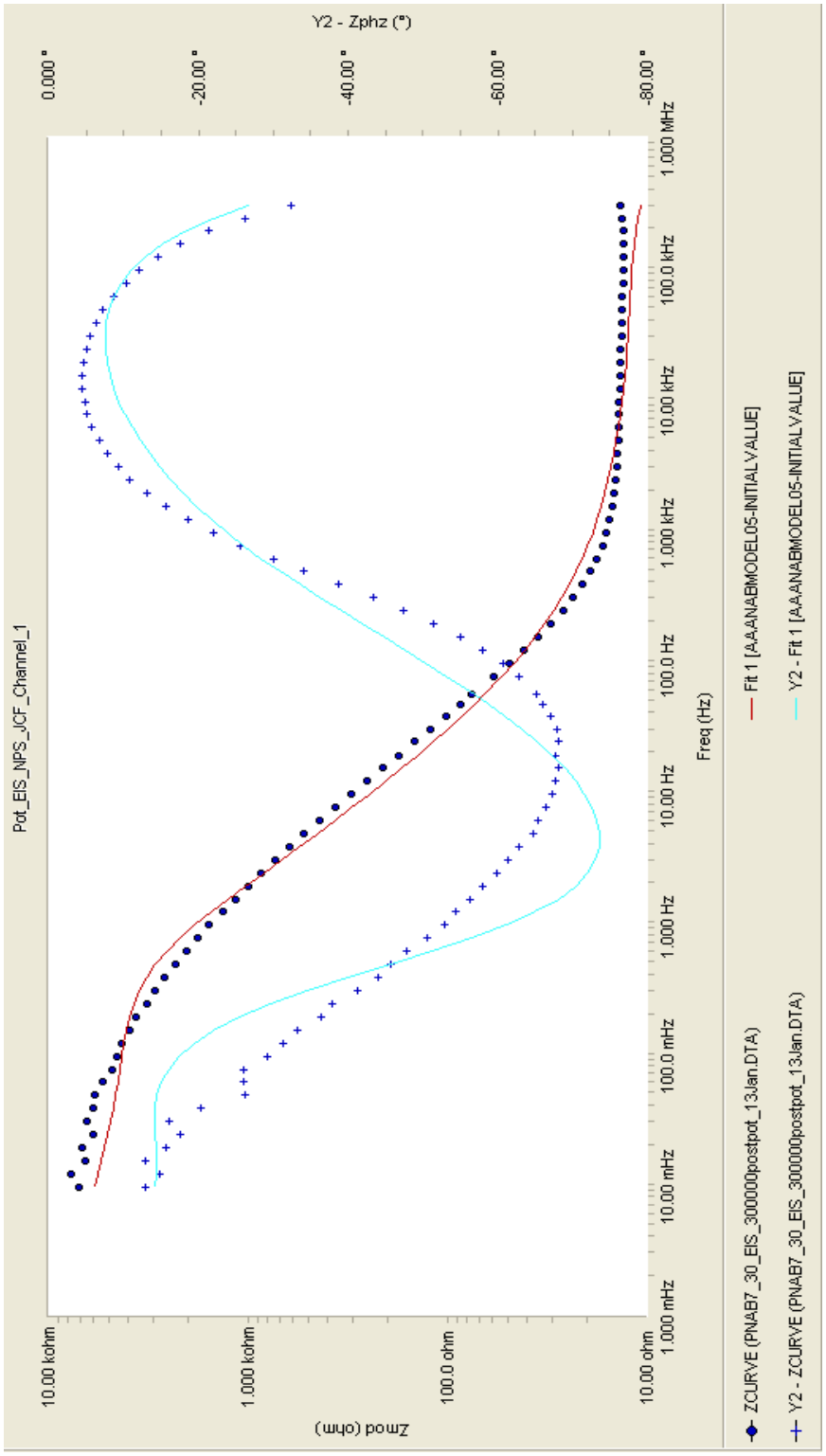

Figure 37: FSP NAB SW 30˚C model 5, three RC series

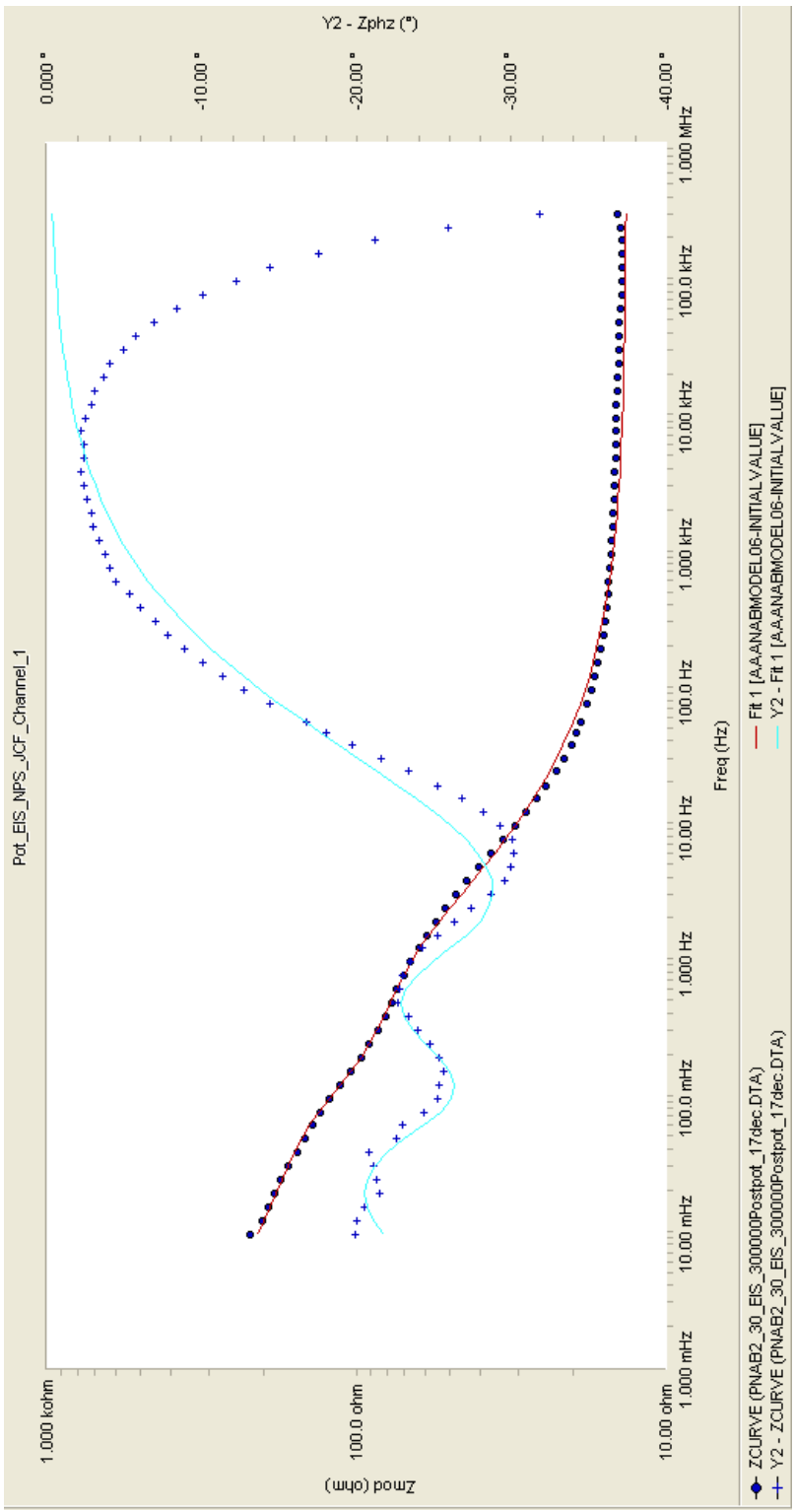

Figure 41: AC (2) NAB SW 30˚C model-6, three RC parallel

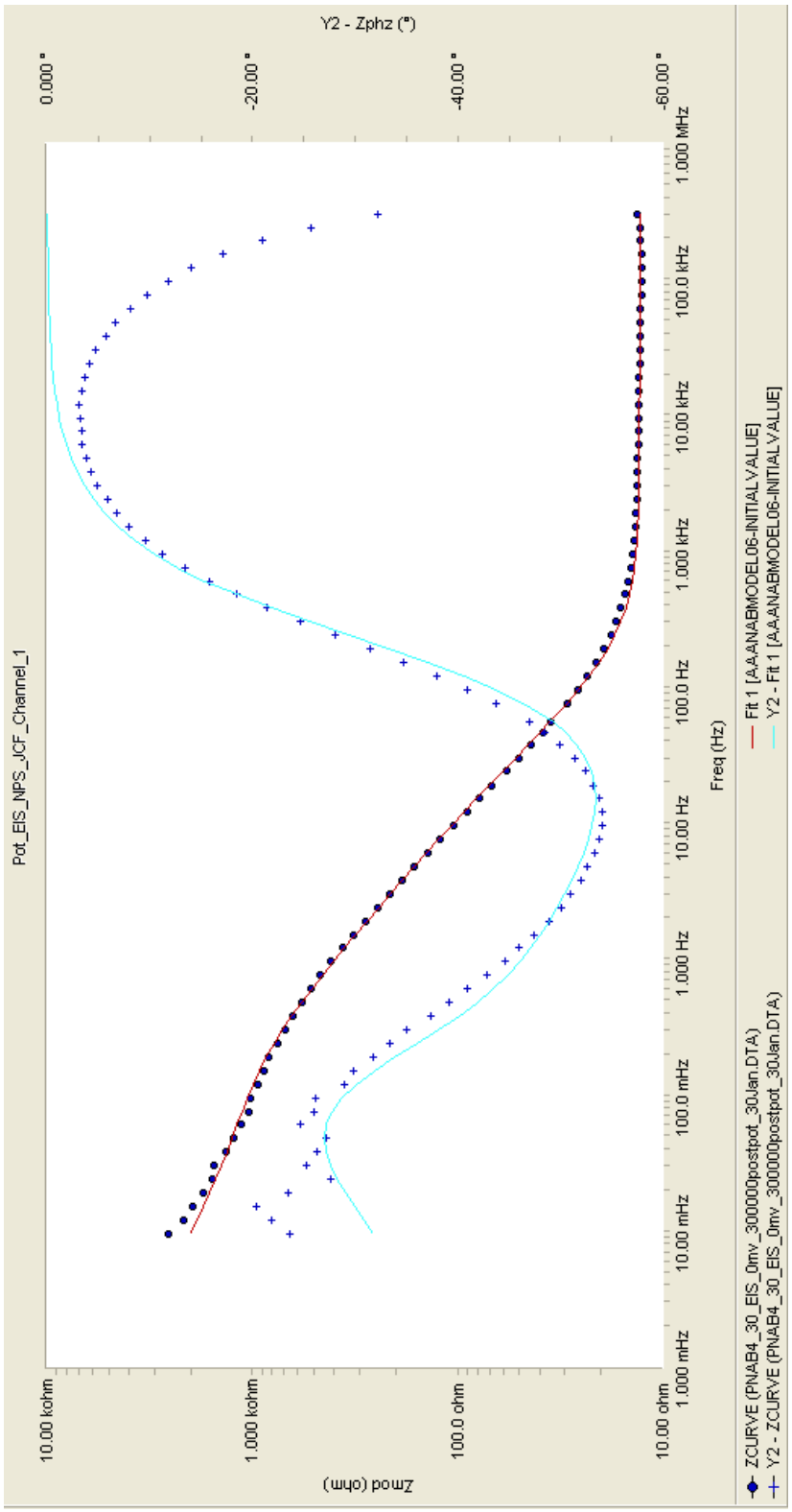

Figure 42: FSP (4) NAB SW 30˚C model-6, three RC parallel

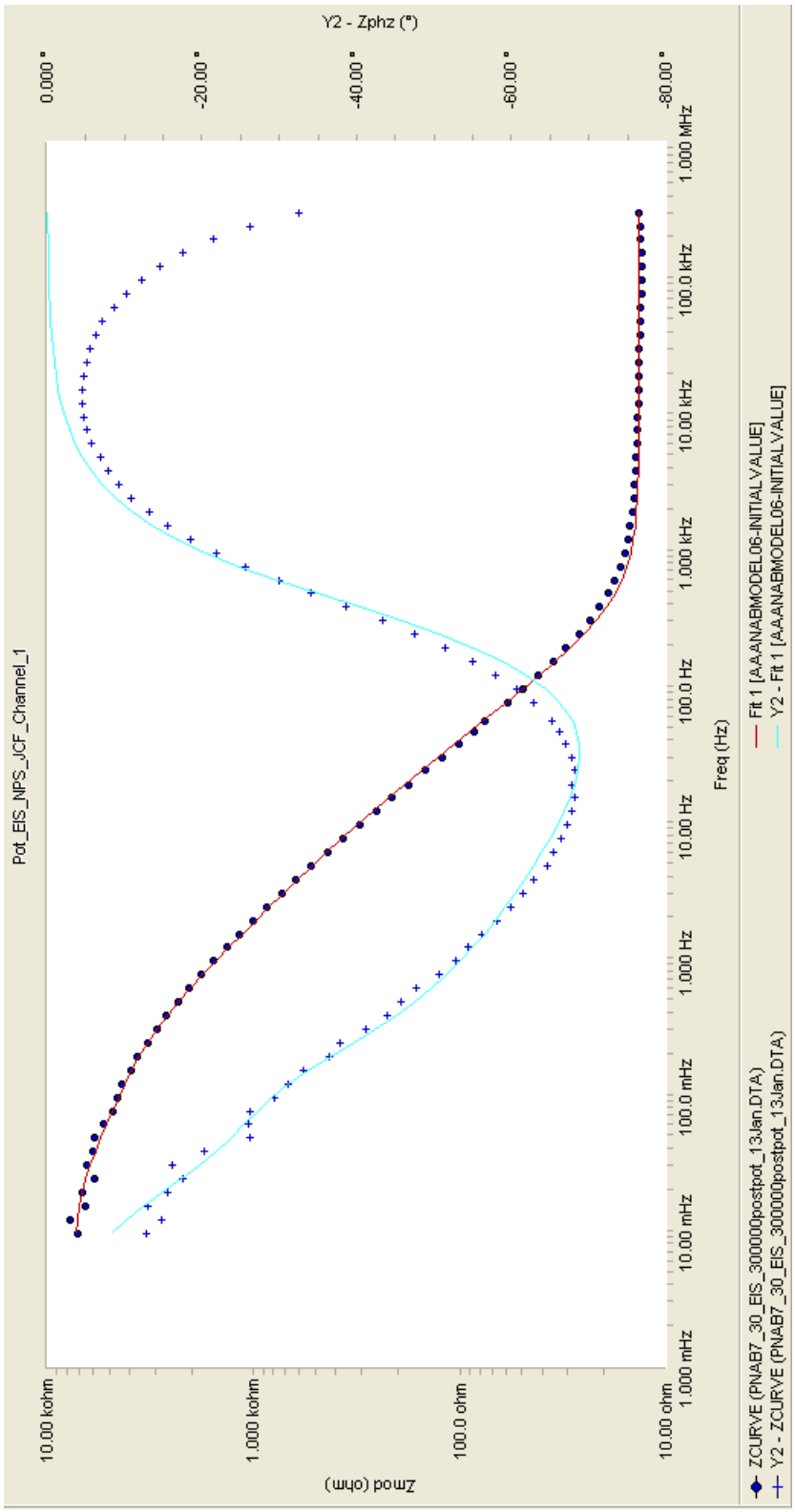

Figure 43: FSP (7) NAB SW 30˚C model-6, three RC parallel

THIS PAGE INTENTIONALLY LEFT BLANK

INITIAL DISTRIBUTION LIST

1. Defense Technical Information Center
   Ft. Belvoir, Virginia

2. Dudley Knox Library
   Naval Postgraduate School
   Monterey, California

3. Dr. Joseph Farmer
   Lawerence Livermoore National Lab
   Livermoore, California

4. Dr. Luke Brewer
   Naval Postgraduate School
   Monterey, California